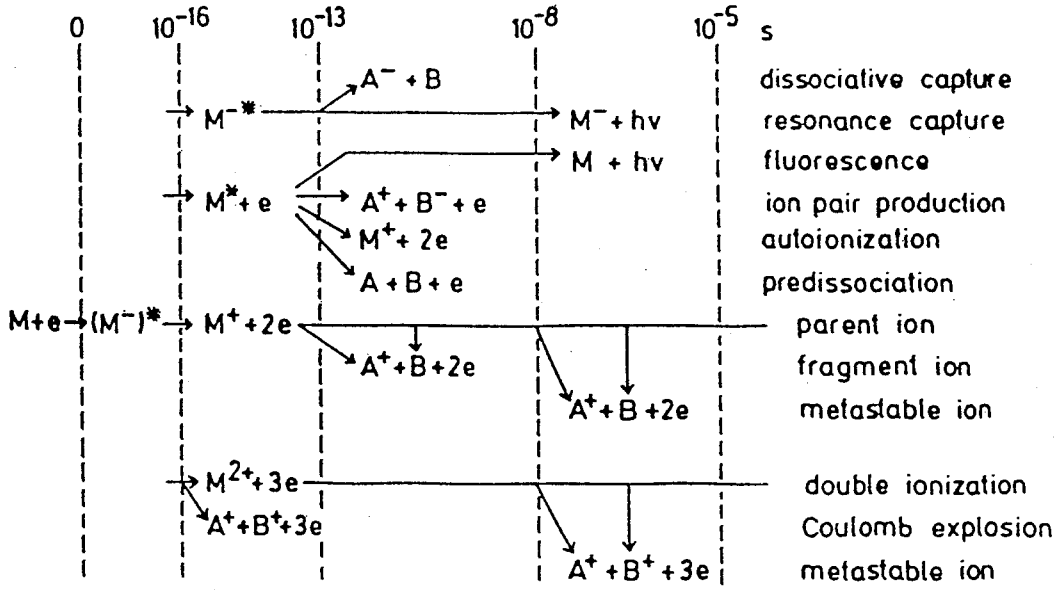

Fig. 3.1. Schematic time chart of possible electron impact ionization processes (after Märk, 1986).

The two curves in the middle illustrate the variation of the strengths of the autoionization processes involving the 3d and 4p electrons. The bottom curve shows the behavior of the direct ionization mechanism (see reaction 3.1).

Multiply charged ions can be formed in a two-step autoionization process. First, a singly charged ion is produced by the ejection of an electron from an inner shell (process 3.4). This internally ionized atom or molecule may then be transformed into a multiply charged ion (reaction 3.7) by a series of radiationless transitions (autoionization or the Auger effect). Figure 3.3 shows as an example the ionization cross section curve for the production of N_2^{2+}, which demonstrates the effect of the Auger process at an incident electron energy of about 430 eV.

For more information on ionization mechanisms and processes see Märk (1982a, 1982b, 1984, 1986; 1994), Massey and Burhop (1969), Field and Franklin (1970), Märk and Dunn (1985) and Illenberger and Momigny (1992). The kinematics of electron impact ionization as described in terms of differential cross sections will be introduced and discussed in detail in Section 3.6. See also Märk (1984) and references given therein.

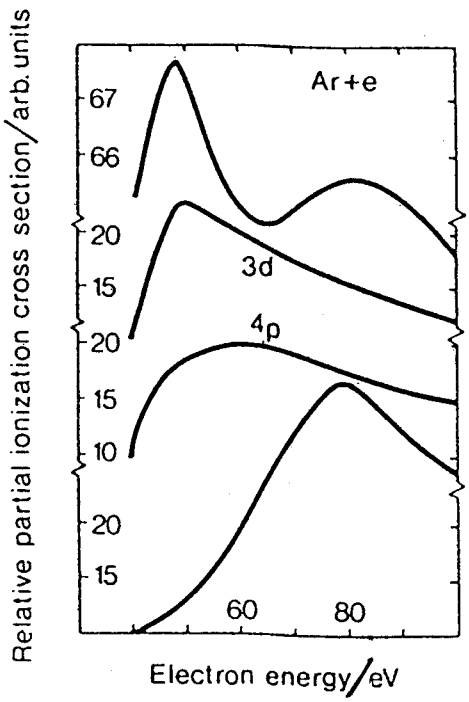

Fig. 3.2. Partial ionization cross section function for $Ar + e \rightarrow Ar^+ + 2e$. Middle curves illustrate the variation of the strengths of the 3d and 4p autoionization features (see text). Bottom curve shows the efficiency of production of Ar^+ via direct ionization processes. Top curve is the sum of the two middle curves and the bottom curve (after Crowe *et al.*, 1972).

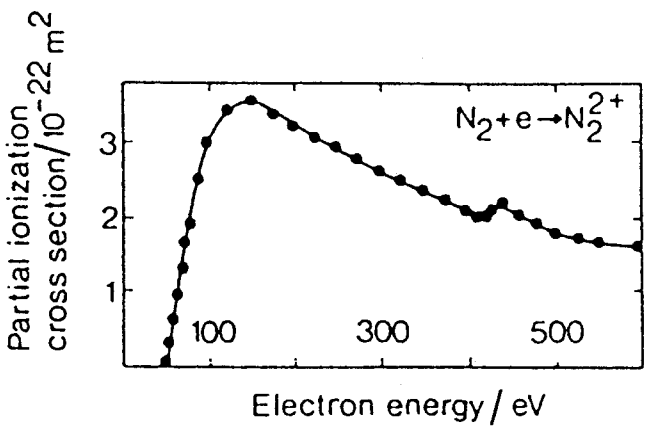

Fig. 3.3. Partial electron impact ionization cross section function for the reaction $N_2 + e \rightarrow N_2^{2+} + 3e$ (after Halas and Adamczyk, 1972/73).

3.3 Total Ionization Cross Sections

3.3.1 Experimental Methods

According to Eq. 1.1 the determination of the total ionization cross section (TICS) σ_i requires the measurement of four quantities, N_e, N_0, n and L. Kieffer and Dunn (1966) have given an extensive discussion of the problems encountered in measuring accurate experimental σ_i values. Also see the more recent reviews by de Heer and Inokuti (1985) and by Märk (1992).

One of the earliest and most widely used experimental methods for determining TICSs is the condenser-plate method of Tate and Smith (1932). This method was used very successfully by Rapp and Englander-Golden (1965) to produce their benchmark TICS functions for the rare gases and several small molecules. In this apparatus, shown in Figure 3.4, a magnetically collimated electron beam is directed through a target gas of known density n. All ions produced in a well defined region are collected on plate P_1. The largest source of error in this method is the measurement of the gas density, a difficult matter for many gases. Djuric *et al.* (1988; 1989; 1991) overcame some of the earlier difficulties in absolute gas density measurements by using a capacitance manometer to determine the pressure in their parallel-plate ionization chamber. De Heer and Inokuti (1985), in their definitive review of the determination of TICSs, discussed and summarized experiments and results up to 1985, including those made using a Lozier tube, the summation method, gas filled counters (Rieke and Prepejchal, 1972) and various kinds of crossed-beam methods.

Excellent data on total and partial ionization cross sections have been obtained recently by Freund and co-workers (Freund, 1987; Freund *et al.*, 1990) using a modified crossed-beam method, in which an electron beam is crossed with a fast neutral beam prepared by electron transfer neutralization of a mass-selected ion beam. This approach was first used for direct and dissociative ionization cross-section measurements by Cook and Peterson (1962), Ziegler *et al.* (1982), and by Smith and co-workers (Montague *et al.*, 1984). Extensions by Freund and co-workers have made it a powerful method (see also Tarnovsky and Becker, 1992; 1993). In the fast neutral beam apparatus of Freund *et al.* shown in Figure 3.5, atomic or molecular ions are extracted from a DC discharge, accelerated to 3 keV, and mass-separated by a Wien filter. The ion beam is then neutralized by electron transfer in a gas selected to have an ionization energy resonant with that of the ions. The pressure is adjusted to neutralize several percent of the ions, with the remainder being deflected to a collector. According to Freund the resulting neutral beam has a typical flux of 10^{10} s^{-1}. Its relative value is measured by kinetic electron ejection from a metal surface. For accurate flux measurements, a pyroelectric crystal is used to calibrate the electron ejection coefficient. Ionization is produced by crossing the fast neutral beam with a well characterized electron beam. The resulting ions are steered and focussed with magnetic and electrostratic fields to a hemispherical energy analyzer. This analyzer separates ions of different charge or mass, since all ions retain essentially the same velocity as the 3-keV parent neutral beam. For molecular species, 100% collection of fragments is possible. Ions are finally detected by a channel electron multiplier. The chief advantage of this method is that it permits preparation of a pure beam even of unstable species, and that the high beam velocity permits accurate flux measurements.

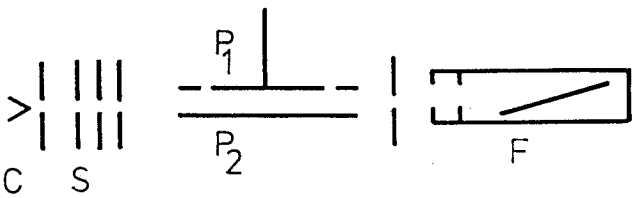

Fig. 3.4. Schematic view of the parallel plate condenser apparatus of Tate and Smith (1932) for the measurement of TICS by electron impact. C, cathode; S, collimator slits; P_1 and P_2, condenser plates; F, Faraday cage. The slanted line inside the Faraday cage is a plate placed at an angle to help prevent reflected electrons from escaping.

3.3.2 Theoretical Methods

Existing theoretical methods for electron impact ionization have been reviewed by Märk (1982a; 1982b; 1984; 1986; 1992), Massey and Burhop (1969), Vriens (1969), Inokuti (1971), Kim (1983a), Younger (1985), and by Younger and Märk (1985). Although most of these treatments apply only to single ionization, they may also be used to estimate TICSs which may also involve multiple ionization. In this section, two very recent theoretical developments will be presented in more detail. The DM approach (Deutsch and Märk, 1987) allows in a very general way the rapid calculation of ionization cross sections as a function of electron energy for targets of ground state and excited atoms, radicals, molecules and clusters. The BED and BEB approach by Kim and Rudd (1994) enables one to calculate SDCSs as well as TICSs but requires in its more accurate (BED) version information on differential oscillator strengths.

Using classical mechanics, Thomson (1912) was the first to derive a formula for the TICS for single ionization;

$$\sigma_i = \sum_i 4\pi a_0^2 N_i \left(\frac{R}{B_i}\right) \frac{t_i - 1}{t_i^2}, \qquad (3.16)$$

with a_0 the Bohr radius, N_i and B_i the number of electrons and the ionization energy in the i-th sub-

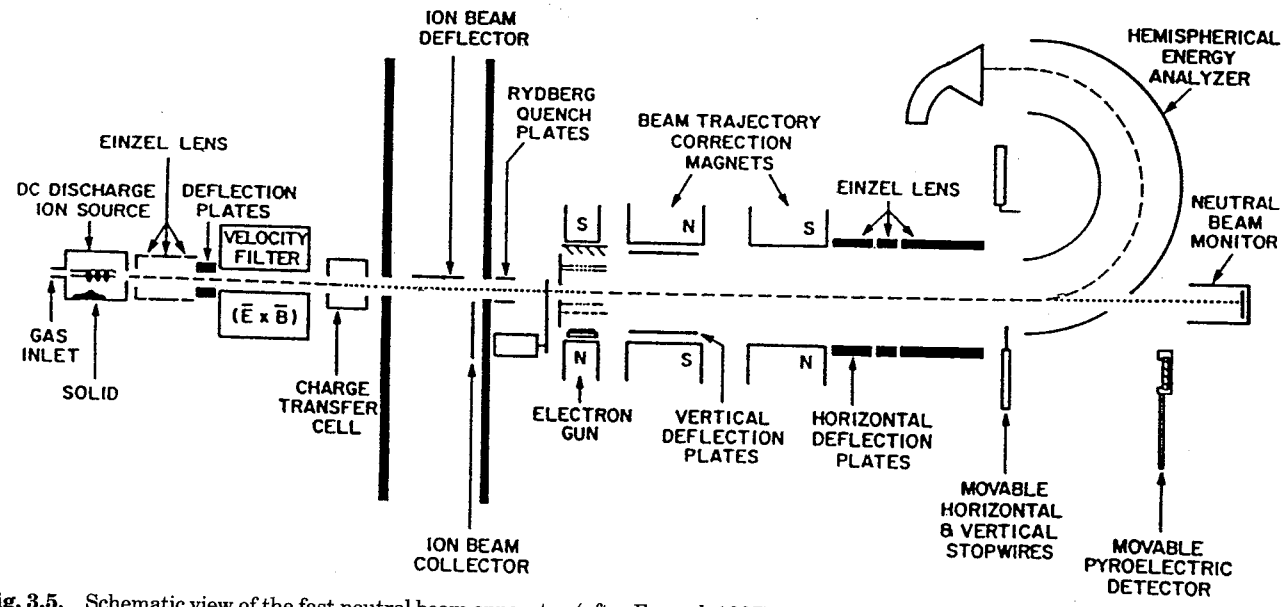

Fig. 3.5. Schematic view of the fast neutral beam apparatus (after Freund, 1987).

shell, respectively, R the Rydberg energy, $t_i = E/B_i$, and E the energy of the incident electron. This classical treatment has been modified by several authors. However, according to Rudge (1968), none of these formulas represents a substantial improvement over the Thomson formula because they all exhibit large deviations from experiment at high and low energies. A definite improvement introduced by Gryzinski (1965) was the assumption of a continuous velocity distribution for atomic electrons, leading to the cross section

$$\sigma_i = \sum_i 4\pi a_0^2 N_i \left(\frac{R}{B_i}\right) \frac{1}{t_i} \left(\frac{t_i - 1}{t_i + 1}\right)^{3/2} \times \left\{1 + \frac{2}{3}\left(1 - \frac{1}{2t_i}\right) \ln\left[2.7 + (t_i - 1)^{1/2}\right]\right\}. \quad (3.17)$$

Burgess (1964) and Vriens (1966) have suggested further improvements in the classical theory by incorporating certain quantal features, *e.g.*, exchange effects. See Section 2.5.2. Although all these classical and semi-classical formulas constitute significant improvements, they still fail in the case of rather simple targets such as neon, nitrogen and fluorine, in predicting the correct magnitude of ionization cross section functions (see examples given by Deutsch *et al.*, 1986 and Deutsch and Märk, 1987). In certain cases, empirical formulas are helpful, but while they provide good fits to certain classes of known data, they are not reliable for other systems. Even the widely used Lotz formula (Lotz, 1967a; 1967b; 1968) fails badly in the case of atoms such as uranium (see Figure 3.6).

Miller and Platzman (1957) gave a simplified equation closely related to Eq. 2.23;

$$\sigma_i = \sum_i \frac{4\pi a_0^2 N_i M_{nl}^2}{T_i} \ln(4c_{nl}T_i), \quad (3.18)$$

where M_{nl} is the dipole matrix element and c_{nl} the collisional parameter determined by Fano plot analyses (see Section 2.13).

Deutsch and Märk (1987) recently suggested replacing the Bohr radius in the Gryzinski formula, Eq. 3.17, by the radius of the corresponding electron subshell. This step is in line (i) with the result of Bethe's calculation that the ionization cross section of an atomic electron with quantum numbers (n,l) is approximately proportional to the mean square ra-

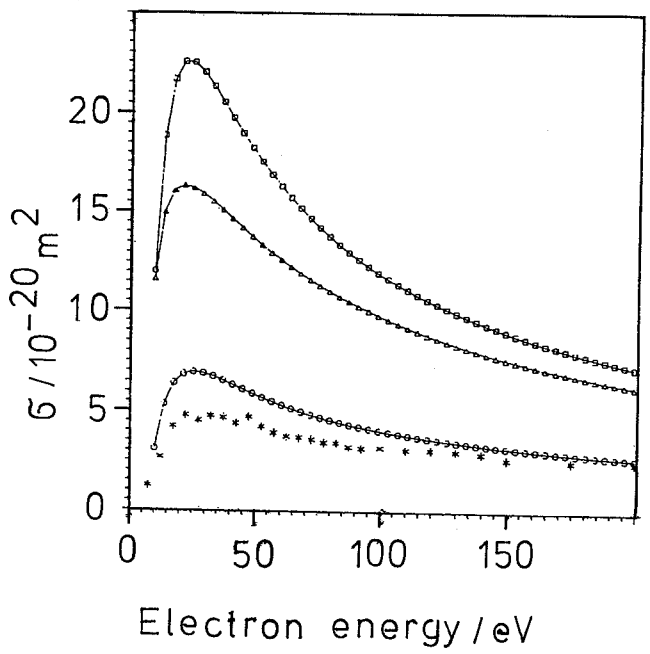

Fig. 3.6. Partial electron impact ionization cross section function for the reaction U + e → U⁺ + 2e. *, experimental results of Halle *et al.* (1981); ○, DM calculations (Margreiter *et al.*, 1994); △, calculations using the Lotz formula; □, calculations using the Gryzinski formula.

dius $<r^2>_{nl}$ of the electron shell (n,l) (Otvos and Stevenson, 1956) and (ii) with the observation of a correlation between the maximum of the atomic cross section and the sum of the mean square radii of all outer electrons (Otvos and Stevenson, 1956; Mann, 1967). Following this suggestion, Margreiter *et al.* (1990a) successfully applied this Deutsch-Margreiter (DM) approach to a large number of ground-state and excited-state atoms using

$$\sigma = \sum_{n,l} g_{nl}\,\pi r_{nl}^2 N_{nl}\,\frac{1}{T_i}\left(\frac{T_i - 1}{u + 1}\right)^{3/2} \times \left\{1 + \frac{2}{3}\left(1 - \frac{1}{2T_i}\right)\right. \times \ln\left[2.7 + (T_i - 1)^{1/2}\right], \qquad (3.19)$$

where r_{nl}^2 is the mean square radius of the nl shell, and the g_{nl} are weighting factors following the original approach of Bethe, 1930, who calculated these "Ionisierungsfaktoren" as a function of the quantum numbers n and l using hydrogenic wave functions. Margreiter *et al.* (1990a) determined the necessary generalized weighting factors g_{nl} (see Figure 3.7) via a fitting procedure using accurate experimental data with the rare gases and uranium as test cases. It was demonstrated that Eq. 3.19 in general leads to an improved agreement with the experimental results not only for ground-state atoms, but also for excited-state atoms (Margreiter *et al.*, 1990a). Recently, Margreiter *et al.* (1994) derived relationships for the product $g_{nl} \cdot B_i$ which yielded even better overall agreement with the experimental data available for atomic targets (see, *e.g.*, Figure 3.6), and also allowed the calculation of ionization cross sections for inner shells (Deutsch *et al.*, 1994) and outer shells (Deutsch and Märk, 1994). Figure 3.8 shows an example of the results for K-shell ionization of Ar.

Kim and Rudd (1994) have recently proposed a method based on the SDCS given in the Mott and

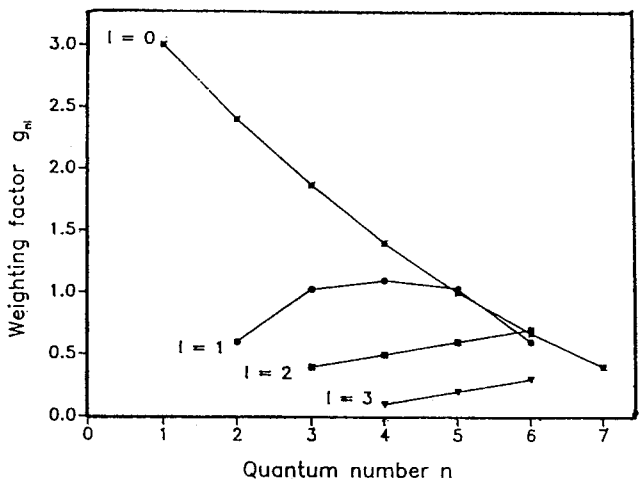

Fig. 3.7. Weighting factors g_{nl} as a function of quantum numbers n and l (after Margreiter *et al*, 1990 a,b).

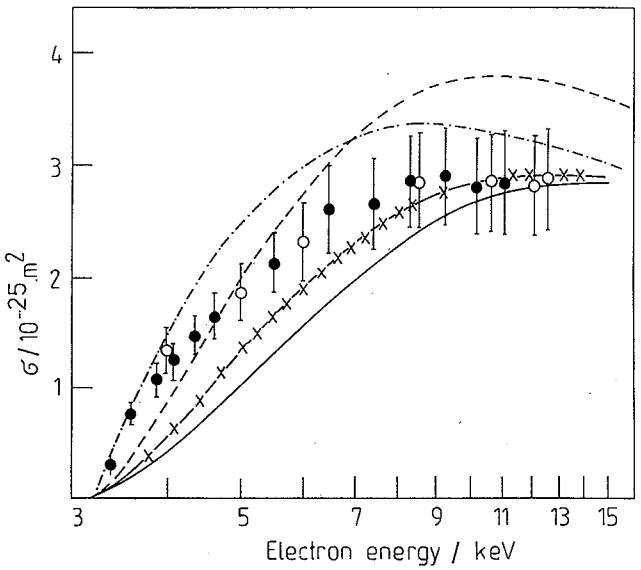

Fig. 3.8. K-shell ionization cross section versus electron energy for argon. ●, experimental results of Hippler *et al.* (1982); ○, experimental results of Tawara *et al.* (1973); dashed line, PWBA calculation of Hippler and Jitschin (1982); dot-dashed line, PWBA Ochkur calculation of Hippler and Jitschin (1982); -×-×-, Coulomb Born exchange calculation of Moores *et al.* (1980); full line, DM approach using a modified Eq. 3.19, Deutsch *et al.* (1994).

BEA formulations. By correcting existing deficiences, *i.e.*, by including the dipole interaction and the quantum mechanically correct high energy dependence as given in the Bethe formula, they developed a SDCS formula which can also be successfully applied, after integration over secondary electron energy, to the prediction of TICSs (*e.g.*, see Figures 3.9 and 3.10). In its simpler version, called BEB, it needs as input data only values of the binding and kinetic energies and occupation numbers for each contributing subshell

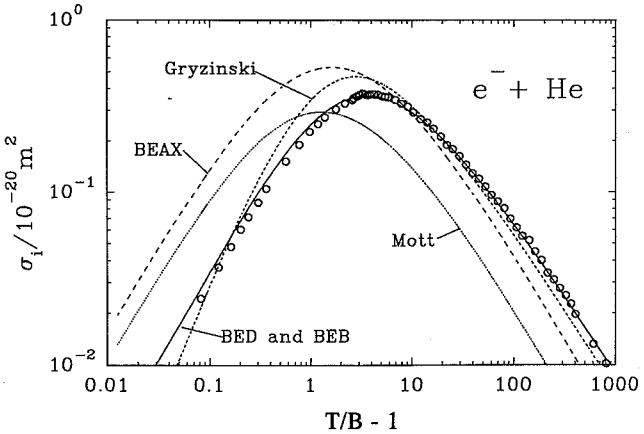

Fig. 3.9. TICS function for electron impact on helium. ○, experimental data of Shah *et al.* (1988) up to 10 keV (above that, the data were generated from the Bethe equation using constants from Kim, 1983a); full line, BED and BEB calculations (both gave essentially the same result); short dashed line, Mott formula, Eq. 2.6; medium dashed line, Gryzinski equation, Eq. 3.17 (Gryzinski, 1965); long dashed line, BEAX (integral of Eq. 2.12).

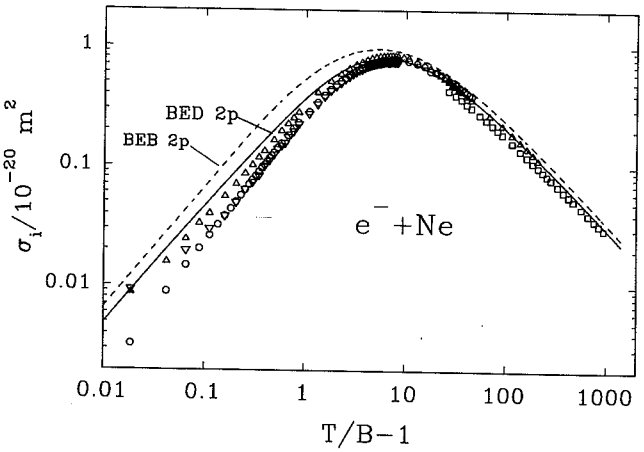

Fig. 3.10. TICS function for electron impact on neon. △, data of Smith (1930); ○, data of Rapp and Englander-Golden (1965); □, data of Schram *et al.* (1965, 1966a); ▽, data of Wetzel *et al.* (1987); full line, BED calculations for the 2p shell; dashed line, BEB calculations for the 2p shell (after Kim and Rudd, 1994).

and the integrated oscillator strength, whereas in its more accurate version called BED information on differential oscillator strengths is also required. The BED and BEB methods are presented in Section 3.6.

Whereas in the case of atoms several approaches at various theoretical levels (quantum mechanical, semiclassical, classical, empirical) exist, in the case of molecules the available theoretical tools are not yet sufficiently accurate or versatile. Some of the classical and semiclassical formulas developed for atoms have been applied with limited success to certain selected cases or classes of molecules such as H_2, hydrocarbons and chlorine compounds (Younger and Märk, 1985; Deutsch and Schmidt, 1984). These formulas fail, however, to predict data for other cases such as molecules containing fluorine (Deutsch *et al.*, 1986; 1989; Deutsch and Schmidt, 1985). Using the concept of the additivity rule, Deutsch *et al.* (1986) recently introduced an empirical correction factor which allows the use of these previous classical and semiclassical theories to calculate ionization cross section functions of molecules containing fluorine and related atoms.

Khare and associates (Jain and Khare, 1976; Khare and Kumar, 1977; 1978) were among the first to suggest a formula specifically designed to allow the calculation of total ionization cross sections of molecules. Recently they have also calculated partial cross sections (Khare *et al.*, 1989). The Jain-Khare formula is based on a semi-empirical combination of the Born-Bethe and the Mott differential cross sections. To use this equation it is necessary to know the differential optical oscillator strengths and the collisional parameters of the molecule under study. This limits the approach of Khare and co-workers (as well as the BED model) to those molecules which have been studied already by photon and/or electron collisions.

Recently, Margreiter *et al.* (1990c) have extended the above mentioned DM approach to molecules using the additivity rule according to which the ionization cross section of a molecule is the sum of the cross sections of the constituent atoms. In order to calculate molecular ionization cross sections with the DM equation (Eq. 3.19) it is essential to identify the corresponding atomic orbitals of the molecular electrons using available Mulliken population analyses of the respective molecules. The main advantage of this DM treatment is that ionization cross sections can be described by a simple analytical formula depending only on basic atomic properties which yields results in better agreement with experimental data than classical, semiclassical or empirical formulas (*e.g.*, see Figure 3.11). Very recently Eq. 3.19 has also been shown to be applicable to radicals (Deutsch *et al.*, 1993) and to clusters (see Märk, 1994 and also Section 3.5). Kim and Rudd (1994) have also recently demonstrated that their model may be used successfully on simple molecular targets such as H_2, N_2 and H_2O (see, *e.g.*, Figure 3.12).

3.3.3 Consistency Checks

Several consistency requirements are described in Section 2.13 and also by Kim (1983b). Some others pertaining to partial ionization cross sections are described next.

In the low energy limit close to the onset of ionization the shape of the partial electron impact ionization cross section curve is governed by a threshold law which is usually expressed in the form

$$\sigma_Z \sim (E - B_i)^{aZ}, \qquad (3.20)$$

where Z is the charge state of the ion and a is a parameter close to 1 (see the discussion by Märk,

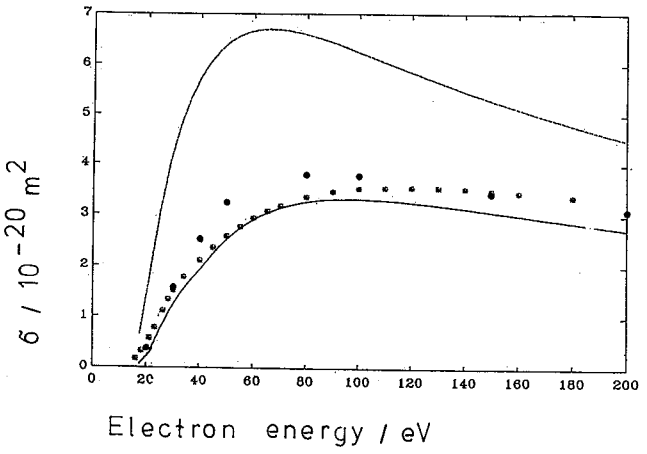

Fig. 3.11. TICS function for electron impact on CO_2. *, data of Rapp and Englander-Golden (1965); ●, calculated cross sections using the Jain and Khare (1976) method; full line, DM formulation of Margreiter *et al.*, (1990c), Eq. 3.19; dashed line, Gryzinski (1965), Eq. 3.17. As described in the text the Gryzinski formula gives erroneous results for molecular targets.

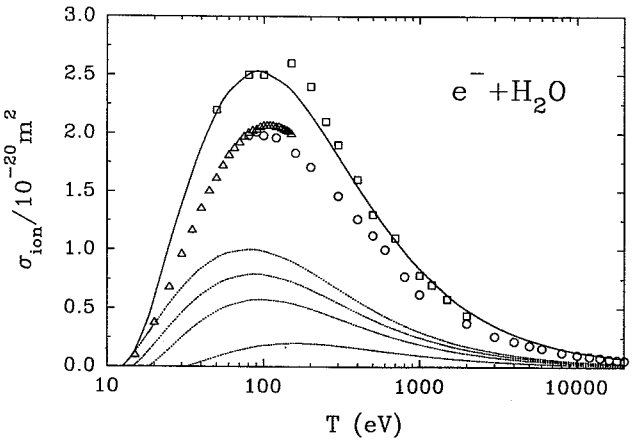

Fig. 3.12. TICS function for electron impact on water vapor. ○, Schutten *et al.* (1966); □, Bolorizadeh and Rudd (1986a); △, Djuric *et al.* (1988); lines, calculations on the BEB model (see Section 3.6.2.2); dotted lines, contributions from the $1b_2$, $3a_1$, $1b_1$, and $2a_1$ subshells; solid line, total.

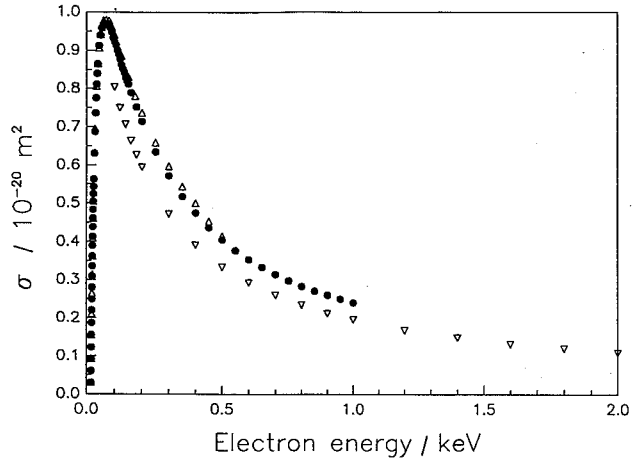

Fig. 3.13. TICS function for electron impact on H_2. ●, Rapp and Englander-Golden (1965); ▽, Schram *et al.* (1965; 1966a) (these data extend up to an electron energy of 20 keV); △, Cowling and Fletcher (1973). Data reported in the MeV range are summarized by McClure (1953) and de Heer (1981).

1984). The precise shape of the cross section in this region is especially important for the determination (by extrapolation) of the respective ionization thresholds, to compare with those derived by other means.

Another important class of consistency checks derives from the fact that the TICS (i) is equal to the charge-weighted sum of the partial ionization cross sections by Eq. 1.3 and (ii) may be obtained by integrating DDCSs over all secondary electron energies and angles. The former condition is used in the summation method (see Section 3.3.1) for calibration purposes and the latter fact in the use of Platzman plots (see Figure 2.1). Both relationships allow one to check the reliability of the absolute magnitude and the energy dependence of the ionization cross sections under consideration.

3.3.4 Recommended Cross Sections

As mentioned above, there exist several comprehensive reviews of experimental and theoretical cross section determinations (see references given in Sections 3.3.1 and 3.3.2), including also compilations of recommended electron impact TICS data (Kieffer and Dunn, 1966; de Heer, 1981; Märk, 1982a,b, 1992; Bell *et al.*, 1983; Märk and Dunn, 1985; Freund, 1987; Tawara and Kato, 1987; Lennon *et al.*, 1988; Shimamura, 1989; Tawara *et al.*, 1990). It is outside the scope of this review to give a detailed account of all available results. Nevertheless, TICS functions for the targets H, He, Ne, Ar, Kr, Xe, H_2, N_2, O_2, H_2O, CO_2, CH_4, and C_3H_8 have been assessed and the best data sets available at this time are presented for some of them in graphical form in Figures 3.9 through 3.16.

3.4. Partial Ionization Cross Sections

3.4.1 Experimental Methods

According to Eq. 1.2, the determination of partial electron impact ionization cross sections σ_{zi} not only requires the measurement of N_{mz}, n, L and N_0 (as in the case of TICS measurements), but in addition an accurate analysis of ions by their mass-to-charge ratio. In order to measure the partial ion currents, a mass spectrometer must be used. Because of the great difficulty in achieving a reliably known transmission and collection efficiency independent of the mass-to-charge ratio, the primary value of mass spectrom-

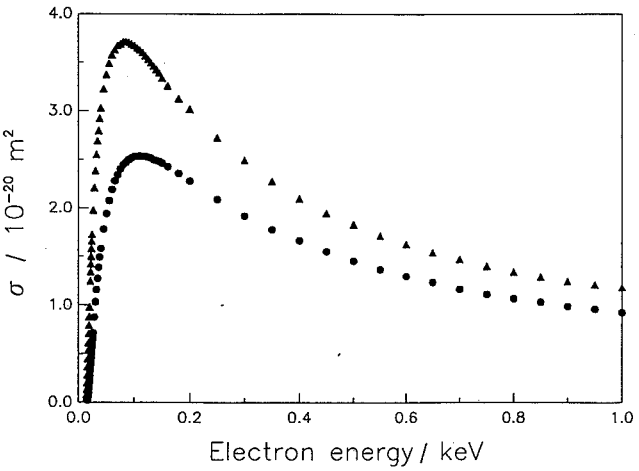

Fig. 3.14. TICS function for electron impact. ●, N_2; ▲, CH_4; after Rapp and Englander-Golden (1965), whose total ionization cross sections are regarded to be the most reliable data sets available. The results (not shown) of Schram *et al.* (1965) for N_2 and of Schram *et al.* (1966b) for CH_4 extend up to an electron energy of 20 keV and 12 keV, respectively. The recent results on CH_4 of Chatham *et al.* (1984) (not shown) are in good agreement with those of Rapp and Englander-Golden (1965).

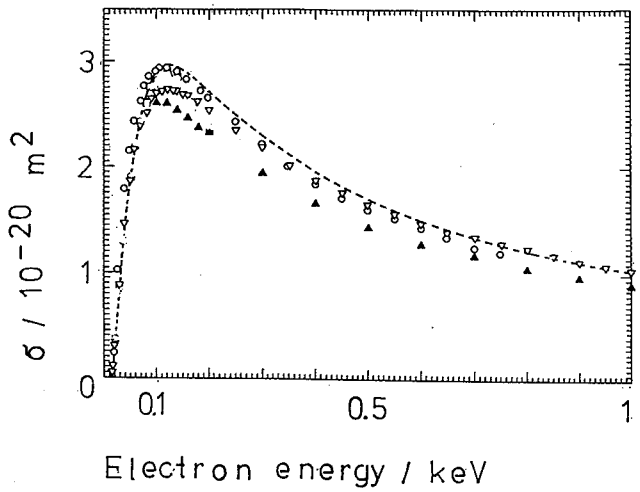

Fig. 3.15. TICS function for electron impact on O_2. ○, Tate and Smith (1932); ▽, Rapp and Englander-Golden (1965); ▲, Schram *et al.* (1965; 1966a); dashed line, Krishnakumar and Srivastava (1992). The data of Schram *et al.* (1965) extend up to an electron energy of 20 keV.

eters has been the identification of different ions produced and the measurement of approximate partial ionization cross section ratios.

The first mass spectrometric determinations of partial electron impact ionization cross section functions were made in the 1930s. Some of these studies were repeated later, however, and large discrepancies were found in both magnitude and shape of the functions. As an example, see the comparison of the cross section ratios between singly and doubly charged argon ions shown in Figure 3.17. As pointed out by many workers (Kieffer and Dunn, 1966; Märk, 1982a;b; 1984; 1985; 1986; Freund, 1987) this is due to large discrimination effects occurring at the ion source exit and at the mass-spectrometer slits, which are discussed in more detail below. Moreover, a common problem which has never been satisfactorily

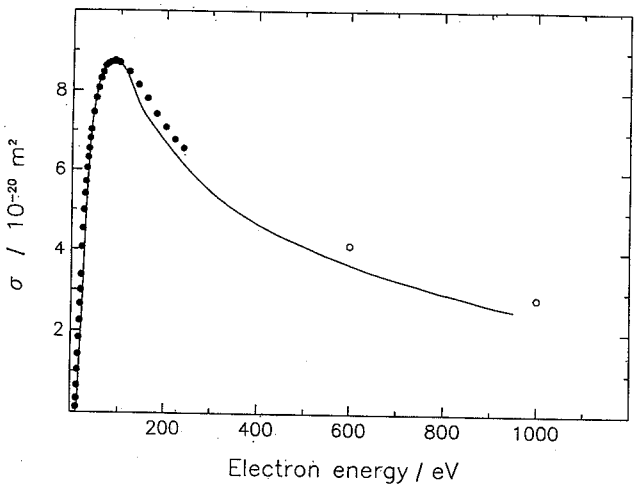

Fig. 3.16. TICS function for electron impact on C_3H_8. ○, Schram *et al.* (1966b) (extending up to an electron energy of 12 keV); ●, Djuric *et al.* (1991); full line, Grill *et al.* (1993a).

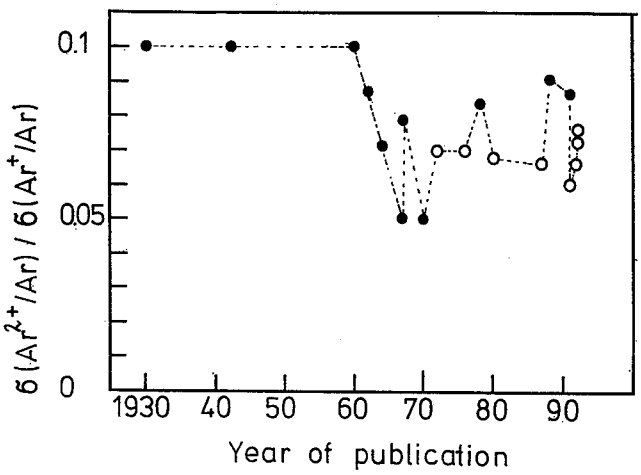

Fig. 3.17. Measured partial ionization cross section ratio $(Ar^{2+}/Ar)/(Ar^{+}/Ar)$ at 100 eV electron energy versus year of publication of these results (original data references given in Margreiter *et al.*, 1990b and Märk 1992). Cross section ratios designated with open circles were measured with improved and controlled experimental conditions (see text) and agree within the experimental error bars. These include the results of Crowe *et al.* (1972), Drewitz (1976), Stephan *et al.* (1980), Wetzel *et al.* (1987), Syage (1991), Bruce and Bonham (1992), Tarnovsky and Becker (1992) and McCallion *et al.* (1992).

solved is that of absolute calibration. Closely related to this is the possibility that discrimination may also occur at the ion detector (see Syage, 1991 and Aumayr *et al.*, 1993 and references therein).

There exist, however, some recent experimental studies using new and sophisticated approaches in order to overcome these difficulties. Some of these new studies come very close to meeting the main prerequisites for measuring accurate partial ionization cross section functions, *i.e.*, a constant, known or complete ion source-mass spectrometer collection efficiency independent of (i) the mass-to-charge ratio of the ion under study, (ii) the incident electron energy, and (iii) in some cases also the initial ion kinetic energy. These studies include the following techniques:

1. Improved crossed thermal beam methods (*e.g.*, see Syage, 1991; Defrance *et al.*, 1982; Wendt and Karstensen, 1984)
2. Crossed fast atom beam techniques (*e.g.*, see Cook and Peterson, 1962; Ziegler *et al.*, 1982; Montague *et al.*, 1984; Wetzel *et al.*, 1987; Freund, 1987; Freund *et al.*, 1990; Tarnovsky and Becker, 1992; 1993)
3. Improved metastable ion detection (see Varga *et al.*, 1981; Lebius *et al.*, 1989)
4. Trapped-ion mass spectrometry (*e.g.*, Lifshitz and Gefen, 1980)
5. Improved ion extraction and transmission techniques (also in combination with molecular-beam techniques), *i.e.*, cycloidal mass spectrometry (*e.g.*, see Schutten *et al.*, 1966; Adamczyk *et al.*, 1966; 1972; Halas and Adamczyk, 1972/73),

Fourier transform mass spectrometry (*e.g.*, Haaland, 1990), large acceptance sector-field mass spectrometry (*e.g.*, Nagy *et al.*, 1980), field-free diffusive extraction (*e.g.*, Crowe *et al.*,1972; Crowe and McConkey, 1977), pulsed electron beam and ion extraction technique (*e.g.*, see Shah *et al*, 1987; 1988; Edwards *et al.*, 1988; Krishnakumar and Srivastava, 1988; 1990; 1992; Syage, 1988; 1991; 1992; Ma *et al.*, 1991a; 1991b; Bruce and Bonham, 1992; McCallion *et al.*, 1992;) coincidence techniques (Spekowius and Brehm, 1991; Bruce *et al.*, 1992), and penetrating-field-extraction and ion-beam deflection method (Märk, 1982b; 1992; Stephan *et al.*, 1980; 1985; Stephan and Märk,1984; Leiter *et al.* 1984; 1989; Margreiter *et al.*, 1990b; Poll *et al.*, 1992; Grill *et al.*, 1993a; 1993b).

As an example, the last of these methods which was developed and continually improved over the past 10 years by Märk and co-workers, employs a Nier-type ion source in combination with a sector-field mass spectrometer (*e.g.*, see Figure 3.18). This system will be discussed in detail in the following paragraph because of the widespread use of this system in mass spectrometer laboratories and its recent success in the determination of accurate partial ionization cross section functions for atoms and molecules. For a detailed and critical discussion of the other very recent and successful approaches, consult the references given above.

Under the usual experimental conditions the extraction of ions from the ionization region in a Nier-type ion source depends on various parameters such as the initial energy of the ions, the mass-to-charge ratio, the guiding magnetic field, the electron-beam space charge, and the applied extraction field. Usually, ions are extracted from the ionization region (in which there are crossed electric and magnetic fields) by a weak electric field applied between the collision chamber exit slit and an electrode opposite to the exit slit

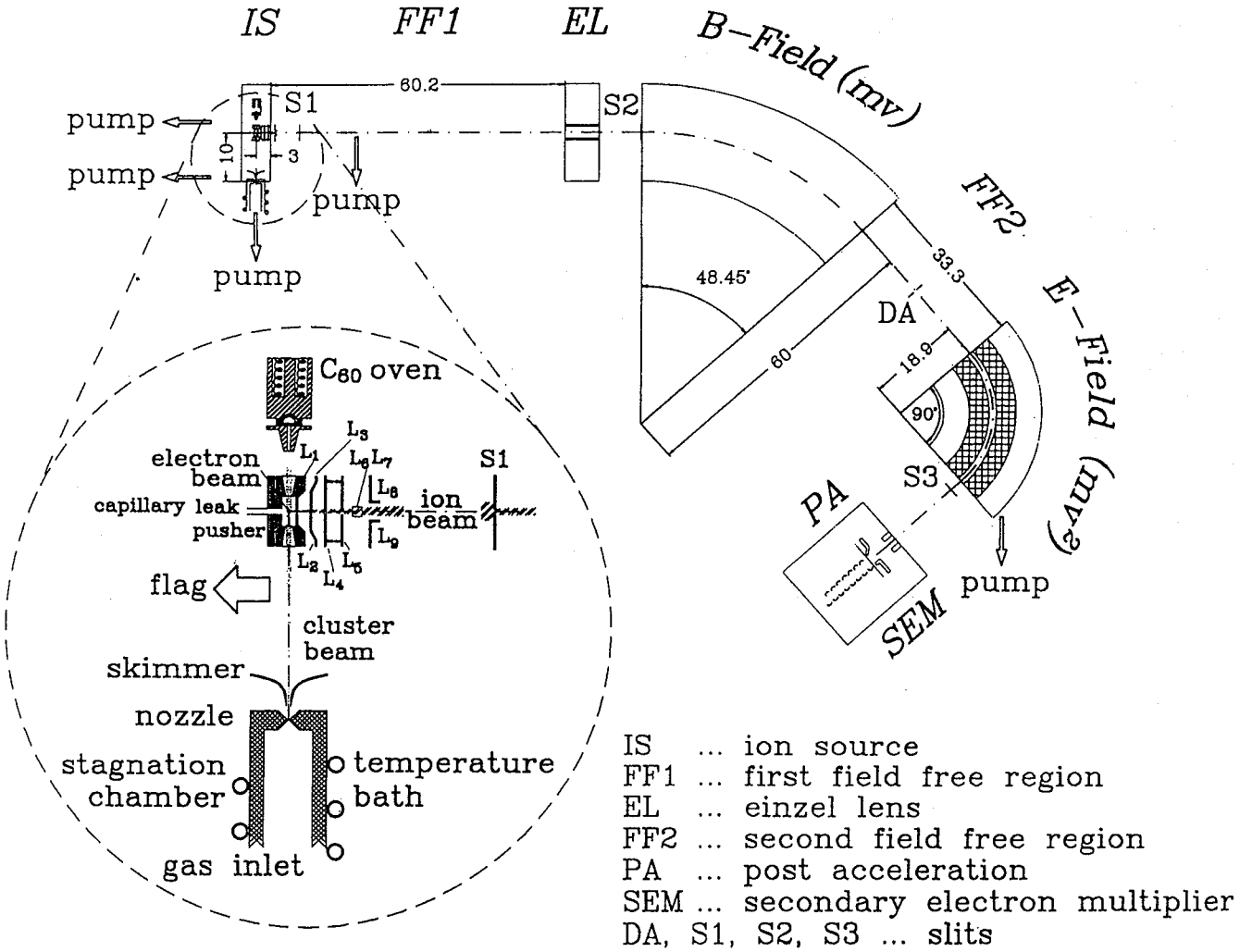

Fig. 3.18. View (to scale, numbers given in cm) of the electron impact ion source and of the double focusing mass spectrometer system. L_1, collision chamber exit slit electrodes; L_2, penetrating field electrodes; L_3 and L_4, focussing electrodes; L_5, ground slit; L_7, L_8 ion beam deflection electrodes; S_1, mass spectrometer entrance slit; *z*-direction: perpendicular to the *x*-*y* plane (right-hand axes) (after Grill *et al.*, 1993a). The magnetic field separates ions according to their momenta and the electric field according to their kinetic energies.

(*i.e.*, a pusher). This extraction, however, is not complete and results in discrimination among ions of different mass-to-charge ratio (*e.g.*, see the detailed discussions by Märk, 1982a; 1982b; 1984; 1985; Kiefer and Dunn, 1966).

In an alternative approach a penetrating field from external electrodes may be used in which all electrodes confined to the collision chamber are kept at the same potential (*e.g.*, the ion acceleration voltage of 3 kV), and ions are drawn out of the collision chamber through the ion source exit slit under the action of an electric field applied to the external electrodes (see Figure 3.18). It has been shown that this penetrating field extraction assures saturation of the parent ion current (Stephan *et al.*, 1980). Ions extracted in this manner are then centered and focussed by various elements and reach the end of the acceleration region at the so-called earth slit. Stephan *et al.* (1980) also introduced pairs of deflection plates (L_6-L_9 in Figure 3.18) in front of the mass spectrometer entrance slit S_1, which serve to sweep the ion beam across the mass spectrometer entrance slit S_1 both perpendicular (y) and parallel (z) to S_1. This allows for the recording and/or integration of the ion beam profile, thus avoiding discrimination at S_1.

This technique has recently been extended to the quantitative detection of fragment ions. Stephan *et al.* (1985) have shown for CF_4 that the overall ion beam shapes are essentially a product of the profiles in either direction. In order to account for the overall discrimination at S_1 Stephan *et al.* have demonstrated that it is sufficient to determine separately the profile in the z direction at one particular y value (*e.g.*, $U_y = 0$ V) and the profile in the y direction at one particular z value (*e.g.*, $U_z = 0$ V) and then integrate with the help of these two data sets over the whole beam shape. This integration method was improved by Leiter *et al.* (1989) by operating a 1-kHz sweep generator on the y-deflection plates during the z scan. It was then sufficient to integrate over this y-integrated z-ion-beam profile in order to obtain a representative measure of the total current of the ion under study.

Margreiter *et al.* (1990b) recently introduced an additional correction procedure to account for a discrimination of energetic fragment ions at the ion source exit slits. It was demonstrated in the case of SF_6 that the smaller of the fragment ions (which have the larger excess kinetic energies) are not extracted out of the ion source with the same efficiency as the larger fragment ions despite the experimental improvements employed previously. This new correction procedure is based on a study of the discrimination in the ion source and mass spectrometer by means of computer simulations (Poll *et al.*, 1992). Ion trajectories were calculated in this study as a function of initial kinetic energy, starting position and starting angle in the ion source. Figure 3.19 shows the

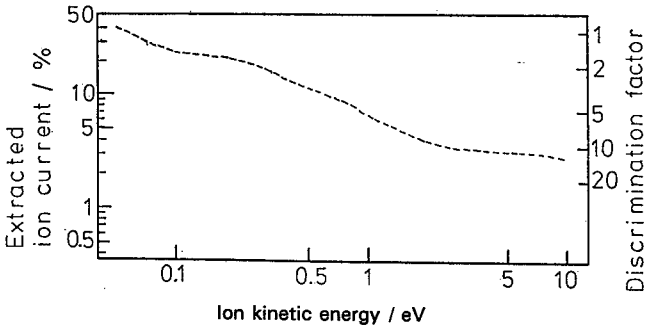

Fig. 3.19. Calculated extracted ion fraction and discrimination factor (see text) as a function of initial ion kinetic energy for a Nier type ion source used in combination with a double focussing mass spectrometer (see Fig. 3.24) (after Poll *et al.*, 1992).

calculated extracted ion fraction as a function of initial kinetic energy. This relationship may be used to correct measured fragment ion currents or, in the case of earlier measurements, partial ionization cross sections. The discrimination factor also shown in Figure 3.19 is defined, according to Poll *et al.* (1992), as the ratio of the fraction of thermal ions extracted to the fraction of ions of all kinetic energies extracted. A representative distribution of the kinetic energies has been obtained in these studies by measuring the z-deflection curves of all fragment ions in comparison to Ar^+ and Ar^{2+} (*e.g.*, see Poll *et al.*, 1992; Grill *et al.*, 1993a; 1993b).

In order to obtain a complete picture of the recent experimental methods, a number of other studies—mostly using quadrupole mass filters or time-of-flight mass spectrometers—should be consulted (see the references given by Märk, 1989).

3.4.2 Theoretical Methods

In contrast to the situation for TICSs few theoretical treatments are available for the calculation of absolute partial ionization cross sections. Besides a few quantum and classical approximations for the production of doubly charged rare-gas atoms (see Figures 16 to 19 in Märk, 1982b), which disagree strongly with experimental results, the only approach for calculating absolute partial ionization cross section functions is the semiempirical formulation by Khare and Meath (1987) and Khare *et al.* (1989). In this approach Khare and co-workers utilized a modified Jain-Khare formula (see Section 3.3.2.) in order to predict the dissociative ionization of small molecules such as H_2O, H_2S and NH_3. Whereas the cross sections for the dominant ions are in good agreement with the experimental results, the theory underestimates the cross sections for minor ions.

In the case of diatomic molecules, another possibility for predicting cross section ratios is the use of the Franck-Condon principle. If the corresponding potential energy curves of the neutral and ionized diatomic

molecule are known, the resulting fragmentation ratios between atomic and diatomic ions may be derived from the calculated normalized vibrational overlap integrals called Franck-Condon factors (see Märk, 1985; 1994 and Levsen, 1978 and references therein). Figure 3.20 shows an example of the calculated and measured results for the H^+/H_2^+ ratio for H_2 as a function of electron energy from threshold up to 25 eV (including, therefore, only contributions from the $^2\Sigma_g^+$ state of H_2^+). The electron impact ionization of large polyatomic molecules also proceeds without nuclear displacement, however the few two-dimensional potential energy curves have to be replaced by a multitude of multi-dimensional potential energy hypersurfaces. Moreover, subsequent dissociation does not occur directly, but only via unimolecular decomposition reactions after the excess energy has been transferred and distributed to many degrees of freedom. In order to describe this ionization and fragmentation process it is possible to use statistical methods, *i.e.* the quasi-equilibrium theory (QET) developed in 1952 or its equivalent the RRKM theory (see Forst, 1973; Levsen, 1978). In the framework of QET, ionization cross section ratios may be derived by (i) determining the rate of dissociation, $k(\epsilon)$, for each fragmentation channel as a function of the internal energy, (ii) constructing the breakdown graph from these individual dissociation rates, and (iii) convoluting this breakdown graph with the total internal energy distribution obtainable from photoelectron spectroscopy, photoionization studies, or from the second derivative of the TICS function. The whole procedure hinges on the assumption of a linear electron ionization threshold law and needs detailed knowledge of the polyatomic compound in terms of vibrational frequencies, activation energies and structure of the transition state. Despite these drawbacks

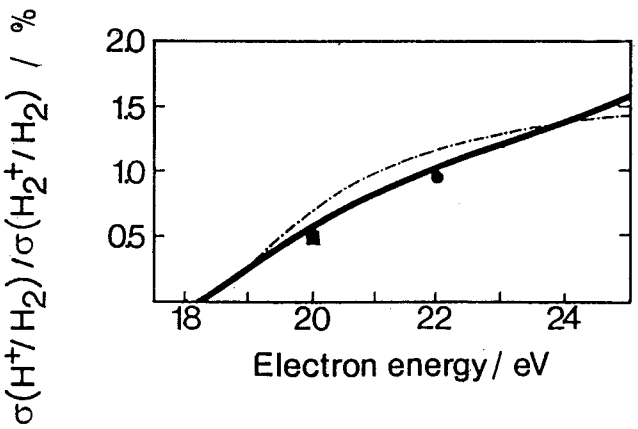

Fig. 3.20. Partial ionization cross section ratio $(H^+/H_2)/(H_2^+/H_2)$ for the electron impact ionization of H_2 as a function of electron energy. ●, Hipple (see Bleakney *et al.*, 1937); ■, Adamczyk *et al.* (1966); full line, Crowe and McConkey (1973a); dash-dot line, predictions by Browning and Fryar (1973) using Frank-Condon factors (see text).

the mass spectra (cross section ratios) of a variety of smaller and also more complex molecules have been calculated (see references given by Märk, 1985; 1994; Levsen, 1978). Figure 3.21 shows experimental and calculated normalized partial cross sections as a function of electron energy for the C_3H_8 molecule as an example.

3.4.3 State-Selected Partial Cross Sections

Most of the partial ionization cross section functions reported in the literature are for ionization of a static target system, *i.e.*, one in thermal equilibrium and in its electronic ground state, into a specific ion distinguished only by charge and mass and not by its electronic state. For a limited number of cases, however, there exist partial cross sections for electron impact ionization reactions taking into account the electronic states of either the neutral target or the ion produced. (For a detailed discussion see Märk, 1985.) In order to illustrate this point, Figure 3.22 shows the corresponding cross section function for the single ionization of metastable neon atoms. The cross section for this metastable atom is approximately one order of magnitude larger than that of the ground-state atom. One may also determine the state-

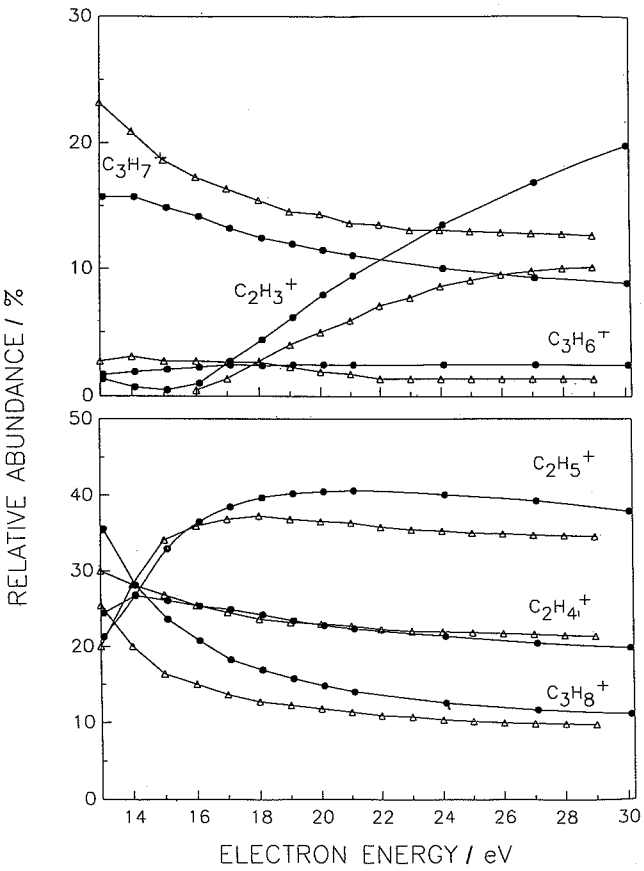

Fig. 3.21. Some relative partial electron impact ionization cross sections for C_3H_8. △, Grill *et al.* (1993a); ●, QET calculations by Vestal (1965) (after Märk, 1994).

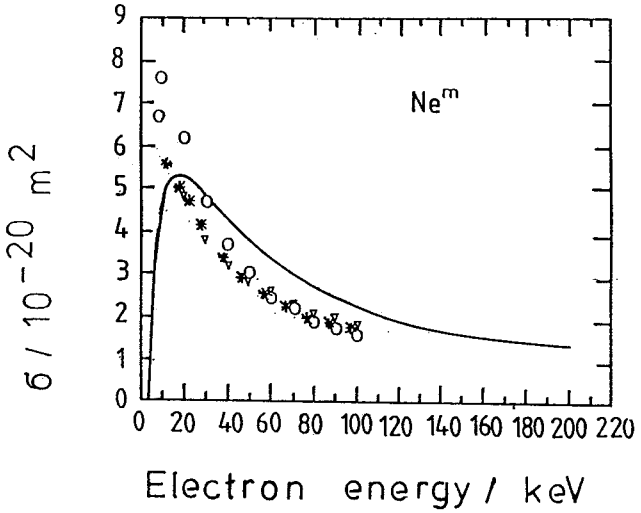

Fig. 3.22. Partial electron impact ionization cross section function for the reaction $Ne^m + e \rightarrow Ne^+ + 2e$ where Ne^m represents the metastable neon atom. *, Dixon *et al.* (1973); ○ Born approximation (Ton-That and Flannery, 1977); ▽, scaled Born approximation (McGuire, 1979); full line, semiclassical DM approach, Eq. 3.19 (Margreiter *et al.*, 1990a).

selected partial cross section for the removal of specific electrons from the target shell in the course of an electron impact ionization process. Typical examples are inner-shell ionization (Figure 3.8) and outer-shell ionization (Deutsch and Märk, 1994).

3.4.4 Recommended Partial Cross Sections

There are a number of comprehensive reviews on partial electron impact ionization cross section determinations including compilations of recommended data (Kieffer and Dunn, 1966; de Heer, 1981; Märk 1982a; 1982b; 1984; 1989; 1992; Bell *et al.*, 1983; Märk and Dunn, 1985; Freund, 1987; Tawara and Kato, 1987; Lennon *et al.*, 1988; Shimamura, 1989; Tawara *et al.*, 1990). As described above, however, the data for partial cross sections are less reliable than those for TICSs due to discrimination effects in the mass spectrometers and ion sources and at the detector in addition to problems arising in the absolute calibration (Märk, 1985). These effects have only been taken into account properly in the past few years. Nevertheless, cross sections for some of the most important targets (*e.g.*, He, Ne, Ar, Kr, Xe, H_2, N_2,O_2, H_2O, CO_2, CH_4, and C_3H_8) have been measured recently with improved methods. The available data on some of these targets have been assessed and reviewed here and the best data sets for some of the targets available at this time are presented in graphical form in Figures 3.17 and 3.20 to 3.28 and in tabular form in Table 3.1.

3.5 Ionization of Clusters

In recent years, there has been a growing interest in a new category of molecules, *i.e.*, clusters. Neutral

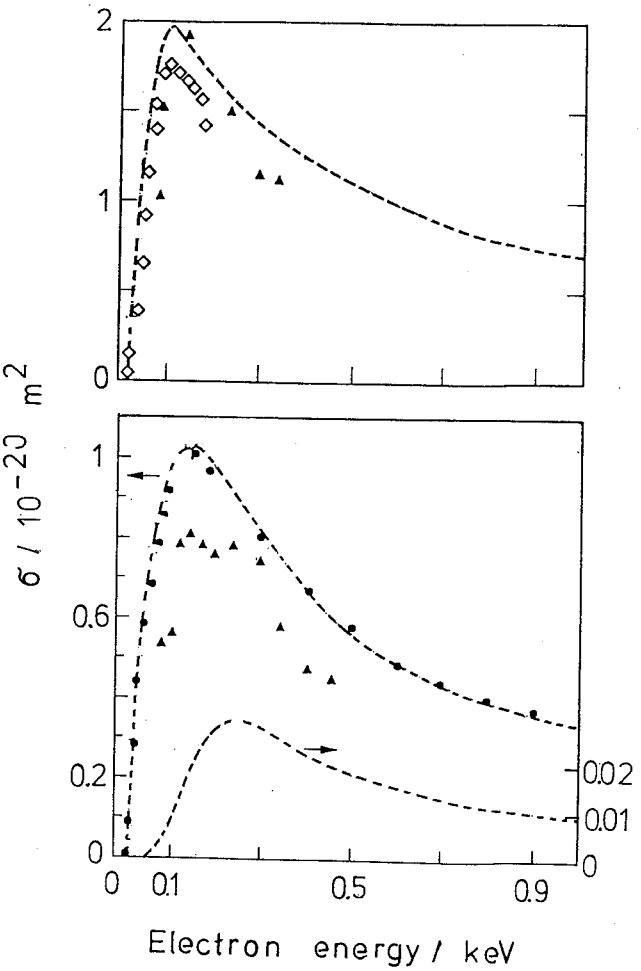

Fig. 3.23. Partial electron impact ionization cross sections function for the reactions $O_2 + e \rightarrow O_2^+ + 2e$ (upper part) and $O_2 + e \rightarrow O^{2+} + 3e$ (lower part, right hand scale) and the production of O_2^{2+} plus O^+ (lower part, left hand scale). ●, Rapp *et al.* (1965); ◇, Märk (1975); ▲, Evans *et al.* (1988); dashed line, Krishnakumar and Srivastava (1992). The data of Rapp *et al.* relate to cross sections for the production of ions with kinetic energies larger than 0.25 eV and can be best compared with the results of other authors for O^+ production. Double ionization of O_2 has been studied and discussed by Märk (see also Table 3.1). Triple ionization has been estimated to amount at 1 keV to appr. 7.1×10^{-4} of the total ionization cross section (Spekowius and Brehm, 1991).

atomic and molecular clusters (bound by weak forces such as dispersion forces) are produced in free jet nozzle expansion, and most of these experiments on so-called van der Waals clusters (Märk, 1987) use electron impact ionization in combination with mass spectrometry for the detection of these species. However, very little quantitative information is available about the ionization cross sections. This is mainly because it is not possible to produce beams of neutral clusters of known density and defined size (Märk, 1987; 1991; Märk and Castleman, 1985).

No absolute total, counting, or partial ionization cross sections for a specific cluster size have been reported except for dimers (see tables given by Märk 1982b; 1987). However, such cross sections have been

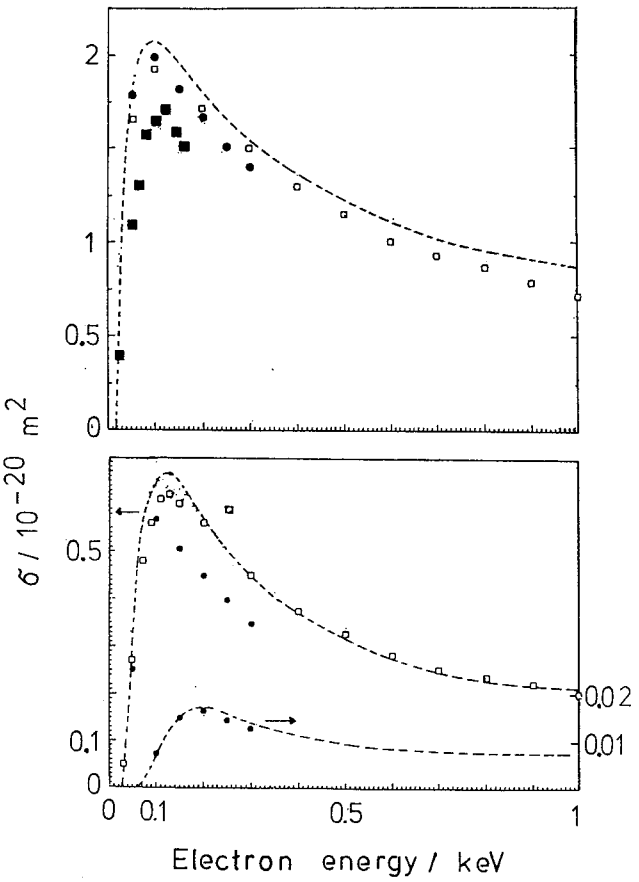

Fig. 3.24. Partial electron impact ionization cross section function for the reactions $N_2 + e \rightarrow N_2^+ + 2e$ (upper part) and $N_2 + e \rightarrow N^{2+} + 3e$ (lower part, right hand scale) and the production of N_2^{2+} plus N^+ (lower part, left hand scale). ●, Crowe and McConkey (1973b); □, Rapp and Englander-Golden (1965) and Rapp *et al.* (1965); ■, Märk (1975); dashed line, Krishnakumar and Srivastava (1990). The data of Rapp *et al.* (lower part) relate to cross sections for the production of ions with kinetic energies larger than 0.25 eV and can be best compared with the results of other authors of N^+ production. Double ionization of N_2 has been studied and discussed by Märk (see also Table 3.1). Triple ionization at 1 keV has been estimated to amount to approximately 7.4×10^{-4} of the total ionization cross section (Spekowius and Brehm, 1991).

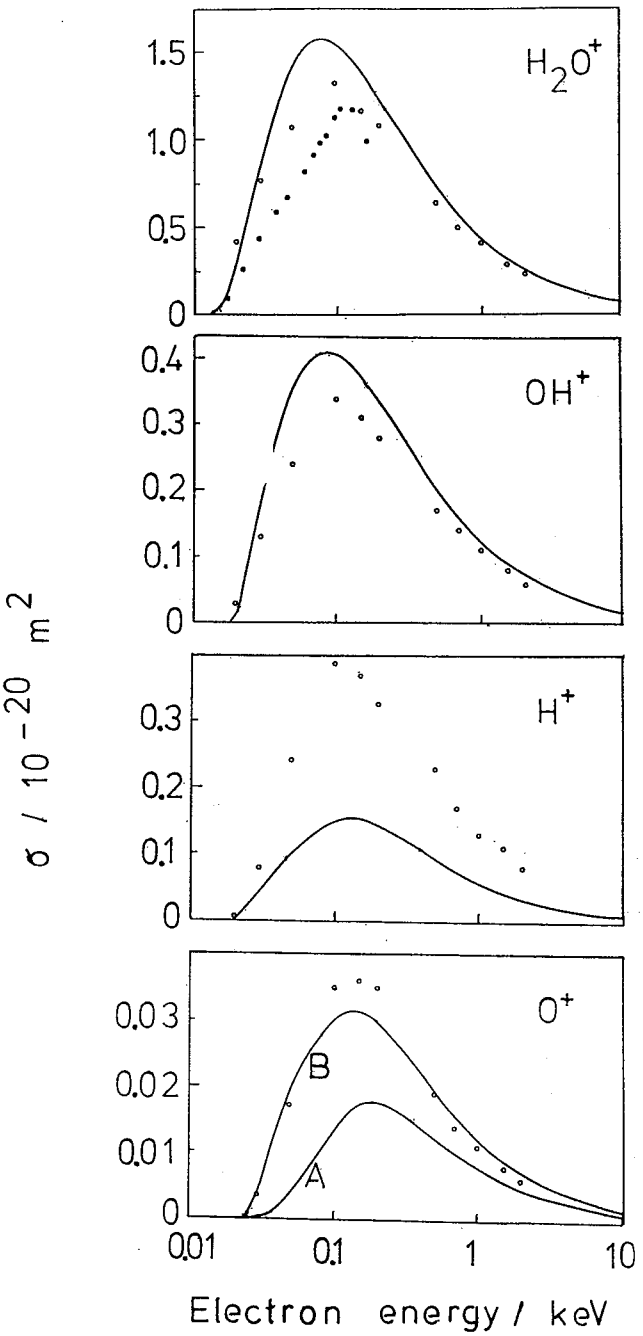

Fig. 3.25. Partial electron impact ionization cross section functions for the reactions $H_2O + e \rightarrow H_2O^+ + 2e$, $H_2O + e \rightarrow OH^+ + H + 2e$, $H_2O + e \rightarrow H^+ +$ products, and $H_2O + e \rightarrow O^+ +$ products. ○, Schutten *et al.* (1966), (for the much smaller production channels concerning the O^{2+} and H_2^+ fragments see Schutten *et al.*); ●, Märk and Egger (1976) for the case of H_2O^+; full line, theoretical estimate of Khare and Meath (1987), (curve A without and curve B with transfer of a certain percentage of the oscillator strengths corresponding to H_2O^+ and OH^+ to those of O^+).

measured for cluster distributions of H_2 and CO_2. For more details, see the references given by Märk (1987). Figures 3.29 and 3.30 show the TICS functions divided by the average number of cluster constituents (the "effective" cross section) for various H_2 and CO_2 cluster distributions. The position of the maximum of the cross section shifts to higher electron energies with larger average cluster size m (due to the loss of energy as the electron passes through the cluster) and the magnitude of the effective cross section decreases for larger m. Also shown in these figures are theoretical estimates using a modified DM approach (Deutsch *et al.*, 1991).

According to theoretical considerations (Keesee *et al.*, 1987) supported by a limited number of experiments, the TICS $\sigma_{i,m}$ as a function of cluster size m may be envisioned to be the product of three probabilities and the TICS of the monomer, $\sigma_{i,1}$:

$$\sigma_{i,m} = \sigma_{i,1} P_1 P_2 P_3, \qquad (3.21)$$

where P_1 is the probability that an electron strikes the cluster. This depends on the geometric cross-sectional area of the cluster and is proportional to

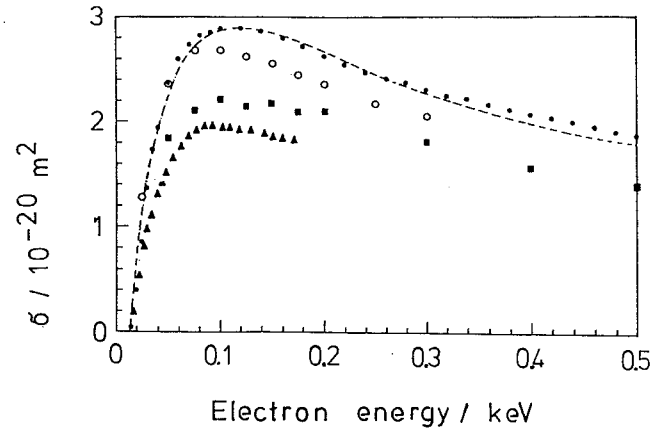

Fig. 3.26. Partial electron impact ionization cross section function for the reaction $CO_2 + e \rightarrow CO_2^+ + 2e$. ■, Adamczyk *et al.* (1972); ○, Crowe and McConkey (1974); △, Märk and Hille (1978); ●, Orient and Srivastava (1987); dashed line, Krishnakumar (1990). Double ionization of CO_2 has been studied by Märk and Hille and other partial cross sections have been reported by Adamczyk *et al.* (1972). Jackson *et al.* (1974) have reported on the influence of the temperature on the dissociative ionization of CO_2.

$m^{2/3}$ for a spherical (or cubic) cluster of m constituents if the density of the cluster is assumed to be independent of cluster size. One must also assume that the cross-section of a molecule within the cluster is the same as that of the free molecule.

The quantity P_2 is the probability that an incident electron can cause an ionizing event within the cluster. This term can be expressed as 1 - exp(-d/l), where d is the mean distance the incident electron travels inside the cluster and l is the mean free path for ionization within the cluster. While l depends only on the energy of the incident electron, d depends on the radial dimension of the cluster and is therefore

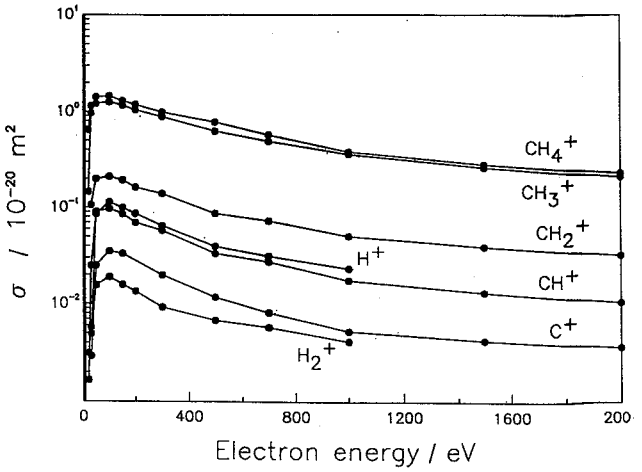

Fig. 3.27. Partial electron impact ionization cross section functions for the reactions $CH_4 + e \rightarrow CH_4^+ + 2e$, $CH_4 + e \rightarrow CH_3^+ + 2e$, $CH_4 + e \rightarrow CH_2^+ + 2e$, $CH_4 + e \rightarrow CH^+ + 2e$, $CH_4 + e \rightarrow C^+ + 2e$, $CH_4 + e \rightarrow H_2^+$ and $CH_4 + e \rightarrow H^+ + 2e$ (after Adamczyk *et al.*, 1966). Neutral products also produced in these reactions are not considered. Similar results have been obtained recently by Chatham *et al.* (1984).

proportional to $m^{1/3}$. Thus, for a small cluster $d \ll l$ and 1 - exp(-d/l) is proportional to $m^{1/3}$, while for a large cluster $d \gg l$ making P_2 unity.

The probability P_3 that the secondary electron escapes the cluster is given by 1-exp(-D/l), where D is the mean distance that a secondary electron can travel in the cluster and still have sufficient energy to escape the cluster. For a small cluster $d \ll D$, and the probability is unity, whereas for a large cluster the probability is proportional to $m^{-1/3}$. Therefore, the total ionization probability for a small cluster ($d \ll l$ or D) is directly proportional to the cluster size m and for a larger cluster (d $\gg$ l or D) the probability is proportional to $m^{2/3}$. The dimension D is expected to be smaller than d, so the expected criterion for this proportionality is $d \gg D$. If the cluster is very large, $d \gg l$ or D, and the proportionality should fall to $m^{1/3}$. Bottiglioni *et al.* (1972) point out that electrons of about 80 eV incident energy can be captured only by clusters exceeding 10^8 molecules.

From the dependence of the total charge production cross section on cluster size (Figures 3.29 and 3.30), Henkes and co-workers determined the ionization shell thickness D to be about three molecular layers for CO_2 clusters (Hagena and Henkes, 1965) and 5.5 layers for the H_2 clusters (Henkes and Mikosch, 1974). In the case of the H_2 clusters, however, the cross sections to be used in the relationship (3.21) were found to be about half of the cross section for the free molecule.

A few relative partial ionization cross section functions have been reported. The most extensive study concerns Ar clusters by Lezius and Märk (1989); others are summarized by Märk (1985; 1987). For the reasons given above no absolute values are available. Owing to this lack of data, the additivity rule (despite being valid only for TICSs) has been occasionally used to calibrate cluster ion signals detected by mass spectrometry, *i.e.*, assuming for instance that the dimer ion signal is twice the monomer ion signal. This procedure, however, is at variance with the results presented above. It neglects possible fragmentation of the neutral under study and possible cascading from larger neutral clusters present in the distributions. Using a modified additivity rule taking into account dissociative channels, it is possible to deduce, at least for rare gas dimers, the absolute partial ionization cross sections (*e.g.*, see the tables given by Märk, 1982b). Moreover, in a few cases accurate partial ionization cross section ratios have been determined for small clusters using either spectroscopic methods (Gough and Miller, 1982; Geraedts *et al.*, 1982) or the method of producing size-selected neutral clusters by momentum transfer via scattering (Buck, 1988). As expected from the mass spectrometry of ordinary molecules, appreciable fragmentation occurs for some

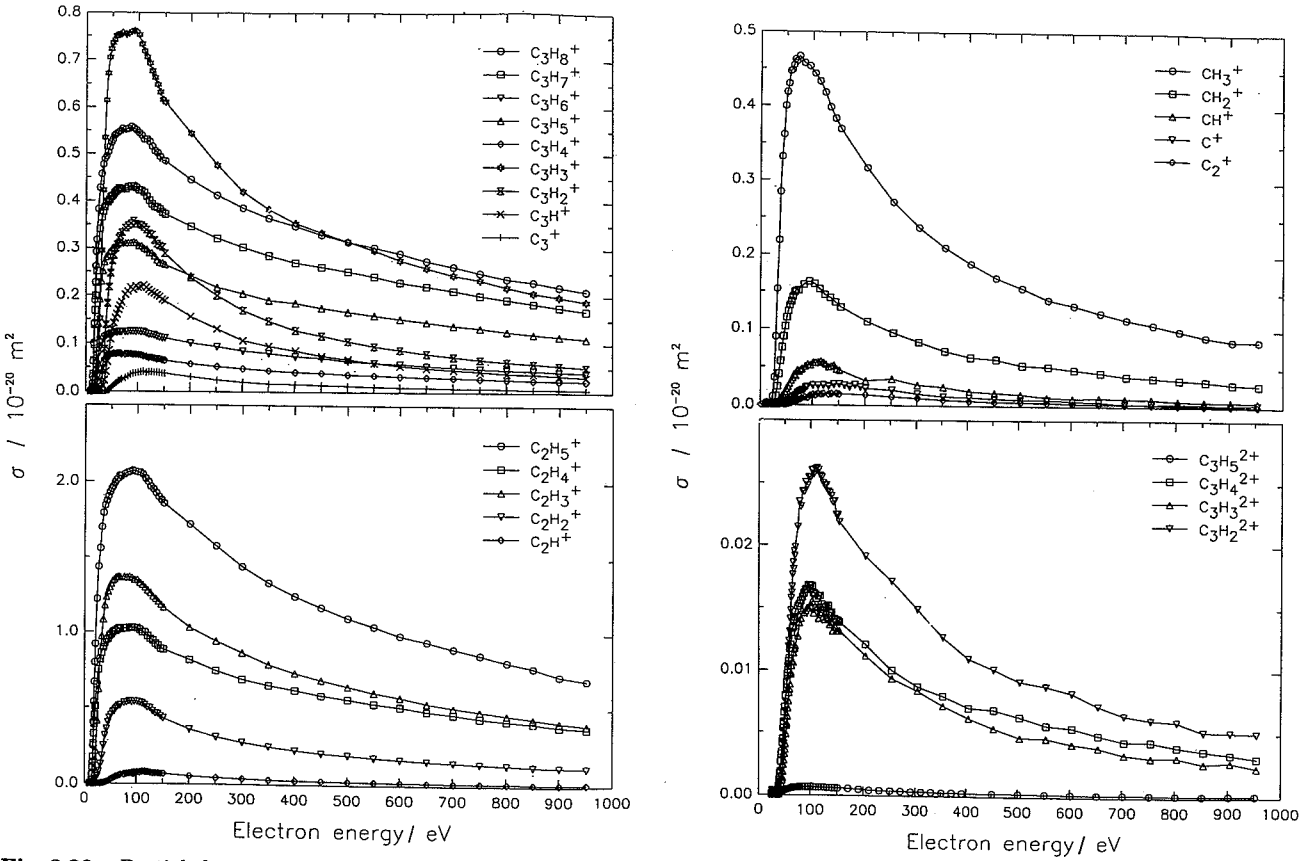

Fig. 3.28. Partial electron impact ionization cross section functions for the production of $C_3H_8^+$, $C_3H_7^+$, $C_3H_6^+$, $C_3H_5^+$, $C_3H_4^+$, $C_3H_3^+$, $C_3H_2^+$, C_3H^+, C_3^+; $C_2H_5^+$,$C_2H_4^+$, $C_2H_3^+$, $C_2H_2^+$, C_2H^+, C_2^+; CH_3^+, CH_2^+, CH^+, CH^+, C^+; $C_3H_5^{2+}$, $C_3H_4^{2+}$, $C_3H_3^{2+}$ and $C_3H_2^{2+}$ ions via electron impact ionization of C_3H_8 (after Grill *et al.*, 1993a). See also relative partial cross sections given in 3.21 and corresponding discussion in the text.

of the atomic and molecular van der Waals clusters studied (Märk and Echt, 1994). Due to additional reaction channels in the case of clusters such as multiple electron collisions and post-ionization intermolecular reactions (Märk, 1994), fragmentation patterns of molecular clusters (*e.g.*, hydrocarbons) are quite different from the patterns known for the respective monomer (Foltin *et al.*, 1991; 1992a; 1992b).

For more details and information on the electron impact ionization of clusters, see Märk (1985; 1987; 1991; 1994), Märk and Castleman (1985) and Märk and Echt (1994).

TABLE 3.1—*Partial electron impact ionization cross sections for the reactions $O_2 + e$ $O_2^{2+} + 3e$ and $N_2 + e$ $N_2^{2+} + 3e$ as a function of incident energy E*[a]

E	O_2^{2+}	E	N_2^{2+}
eV	10^{-22} m²	eV	10^{-22} m²
42	0.011	44.5	0.006
44	0.023	46.5	0.028
48	0.045	50	0.11
51.5	0.080	53.5	0.28
53	0.10	57	0.49
62	0.24	60.5	0.76
73	0.41	68.5	1.30
94.5	0.87	78.5	2.17
109	1.02	98.5	2.95
126	1.04	118.5	3.32
139	1.07	124.5	3.35
156	1.04	145.5	3.22
167	1.00	165.5	2.59

[a] After Märk, 1975.

3.6 Differential Ionization Cross Sections

3.6.1 Experimental Methods

The experimental arrangements used in various laboratories to measure the DDCSs all involve a method for producing a narrow, monoenergetic electron beam which passes through a low-density target gas, a method of analyzing the energies of the ejected secondary and/or scattered electrons, and an electron detector. Electrons which are emitted from a short length of the beam into a small range of angles and within a narrow range of energies are detected during the same period of time that the primary beam is collected and integrated. The DDCS, $\sigma(\epsilon,\theta)$, is defined in Section 1.2.

With most systems, the output currents are small, so detection is accomplished by a device such as an

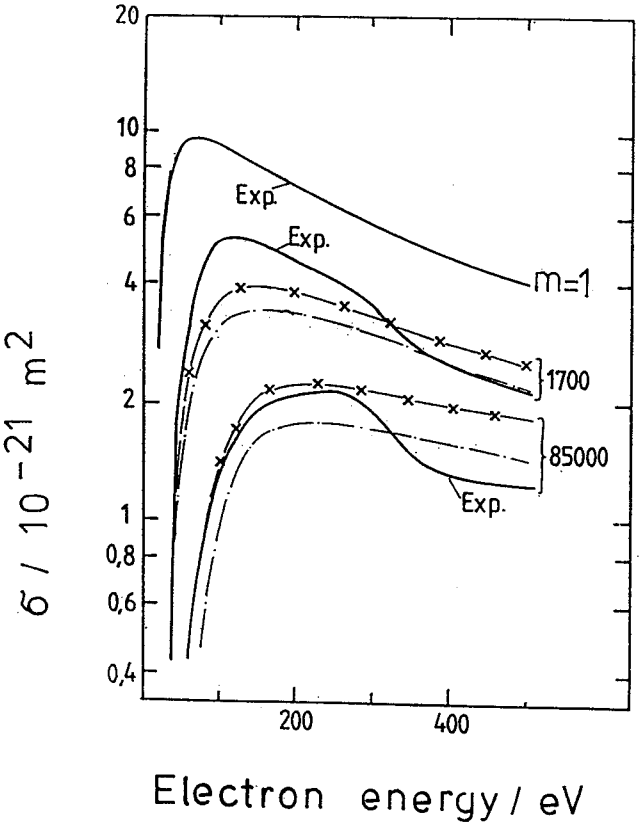

Fig. 3.29. Effective TICS functions for electron impact on various $(H_2)_m$ cluster distributions with an average cluster size m. Full lines designated Exp., Henkes and Mikosch (1974). Calculated values using a modified DM approach (after Deutsch *et al.*, 1991), dash-dot line, a=0.47; -x-x-, a=0.48. In this case r_{nl}, N_{nl} and g_{nl} in Eq. 3.19 have been replaced by $m^a r_{nl}$, mN_{nl} and g_{nl}/m, respectively.

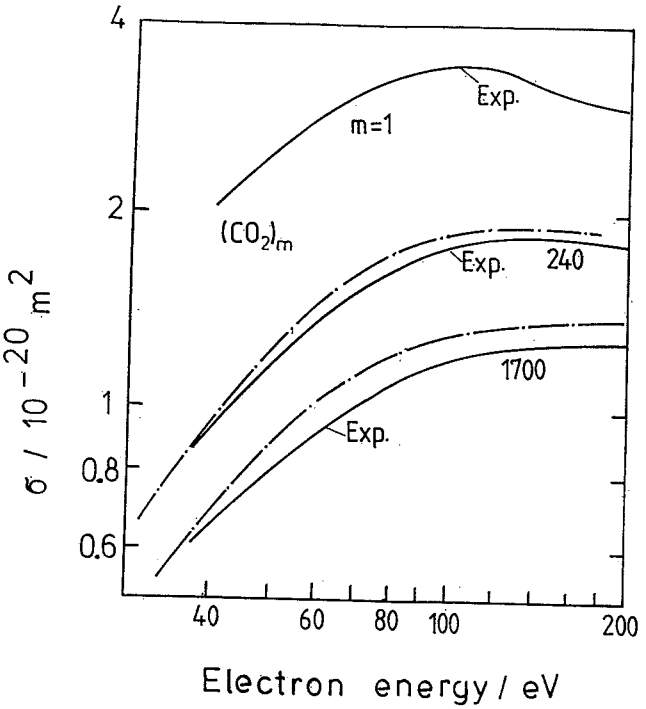

Fig. 3.30. Effective TICS functions for electron impact on various $(CO_2)_m$ cluster distributions with an average cluster size m. Full lines designated Exp., Hagena and Henkes (1965); dash-dot line, calculated values using a modified DM approach with a = 0.41 (after Deutsch *et al.*, 1991, see Figure 3.29).

electron multiplier or channel electron detector which counts individual electrons. The detector efficiency (ratio of the number of countable output pulses to the number of electrons reaching the detector) must be known or measured for accurate work.

The experimental systems that have been used can be classified into three main categories according to their method of energy analysis.

A) Rotatable electrostatic analyzer

Electrons ejected from the target into a small range of angles, typically 1° to 5°, are admitted to the analyzer. An electric field deflects these electrons by various amounts depending on their kinetic energies and an exit slit allows electrons within a narrow range of energies to pass on to the detector. The principal forms of electrostatic analyzers that have been used are the hemispherical, cylindrical, parallel-plate, and cylindrical-mirror types. The resolution $\Delta\epsilon/\epsilon$ of such analyzers is given by a simple function of the slit widths and other geometrical quantities and is typically 1 to 6%. For a description of various types of electrostatic analyzers, their transmission functions and resolutions, see Sevier (1972).

In this system, the ejection energy is selected by choosing the potentials on one or more electrodes of the electrostatic analyzer. By stepping through the proper voltage range, the energy spectrum of electrons is recorded. Either the analyzer or the electron gun is rotatable so that electrons ejected over a range of angles can be selected, thus giving the angular distribution.

As an example, the apparatus used by Peterson *et al.* (1972) for their extensive set of measurements (compiled in Opal *et al.*, 1972) is shown in Figure 3.31. In this system, the electron gun is aimed into a Faraday cup and the combination is rotated together relative to the analyzer-detector assembly. The target is a jet of gas from a capillary tube but some other investigators have used a static target gas. The jet has the advantage of limiting the spatial extent of the target thus reducing the number of spurious electrons reaching the detector. However, it is difficult to determine the density profile of such a target and absolute data taken with a static target are usually needed to normalize the jet data.

B) Rotatable time-of-flight (TOF) analyzer

Goruganthu and Bonham (1986) used a rotatable time-of-flight analyzer to obtain the energy spectra of electrons. In this method, the primary beam current is switched on for a short interval of time by an electric pulse which also starts a ramp voltage. When a secondary electron is detected after travelling a fixed distance, a pulse is produced the size of which is

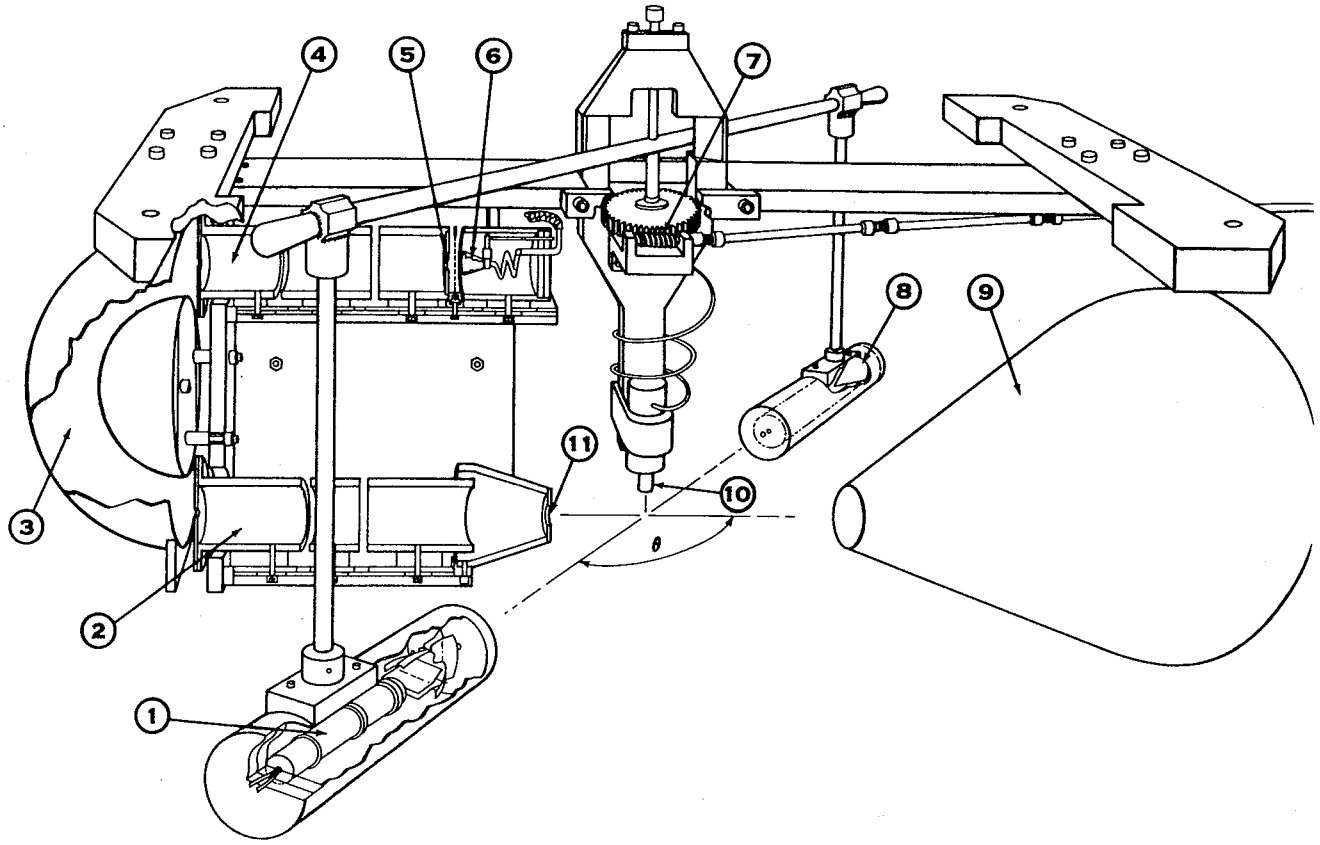

Fig. 3.31. Apparatus used by Peterson *et al.* (1972) to measure cross sections for secondary electron emission in electron-atom collisions. 1, electron gun; 2, input lenses; 3, hemispherical analyzer; 4, output lenses; 5, exit slit; 6, detector; 7, angle drive; 8, Faraday cup; 9, conical trap; 10, gas supply; 11, limiting aperture (from Opal *et al.*, 1971; 1972).

proportional the ramp voltage at that time and therefore to the time of travel. A pulse-height analysis of a large number of such pulses yields a time spectrum which is converted into an energy spectrum. TOF systems have better transmission and resolution at low energies than electrostatic analyzers, but generally require normalization to yield absolute cross sections.

C) Stationary segmented spherical analyzer

McGowan *et al.* (1969) and Vroom and Palmer (1977) developed a differential energy analyzer which consisted of two concentric spherical grids surrounded by a concentric, segmented spherical collector. An electron travelling radially outward from the collision region at the center of the spherical system passes through a retarding field between the grids and is collected by one of the 11 segments which define the angles of ejection of the electron. Because each segment collects electrons emitted over a complete 2π azimuthal angle, current measuring techniques could be used instead of counting methods, however, since each electrode segment subtends a 15° angle, their angular resolution was only ±7.5°. DDCSs are obtained by differentiating the electron retarding spectra and normalizing to data taken by other methods.

Grissom *et al.* (1972) used an altogether different sort of apparatus to obtain the SDCSs for secondary electron emission near zero energy. This was done by the trapped-electron method in which slow electrons from a target were trapped in a potential well. Such measurements provide cross sections in the very low secondary electron energy region which is difficult to reach by other means.

Although there is general agreement among the cross sections measured by the various researchers, there are also areas of disagreement. Figure 3.32 shows a typical comparison of angular distributions. The cross sections of Opal *et al.* (1971; 1972) tend to be smaller than the others at their extreme angles 30° and 150°. This has been attributed (Rudd and DuBois, 1977) to the assumption of Peterson, *et al.* (1972) that the density in their target gas beam is uniform over the entire length of path viewed by their analyzer. Fortunately, this had little effect on their SDCSs. Some early data (*e.g.*, Oda, 1975 and Bolorizadeh and Rudd, 1986a) exhibited a marked rise in the angular distributions at very small angles (*e.g.*, 10°), which is probably spurious. In later work, a weak retarding field at the entrance slit of the analyzer was used which largely corrected the problem.

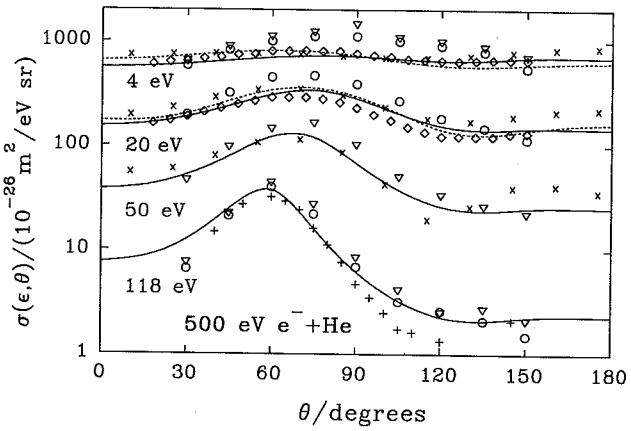

Fig. 3.32. DDCSs from 500-eV e^-+He collisions as a function of angle for various ejected electron energies. Full line, Eq. 3.23; dashed line, recommended values of Kim (1983b); ○, Opal *et al.* (1972); ×, Goruganthu and Bonham (1986); +, Oda (1975), ▽, Sethuraman *et al.* (1972); ◇, Müller-Fiedler *et al.* (1986) (from Rudd, 1991).

3.6.2 Theoretical Methods and Semiempirical Models

Most of the theoretical methods described in Section 2 are applicable to electron impact and several have been used to calculate differential cross sections. However, there has been no systematic comparison of the various theories with experiment for a wide range of primary and secondary energies, angles, and targets.

Experimental data on hydrogen and helium have been compared to calculations made with the Gryzinski equation, the binary encounter model, and the Born approximation by Bell *et al.* (1970), Tahira and Oda (1973), and by Bell and Kingston (1975). Omidvar *et al.* (1972) calculated SDCSs for 11 different atomic targets using plane waves to describe the incident and scattered electrons and screened hydrogenic and Coulomb functions to describe the atomic electrons. Burnett *et al.* (1976) evaluated DDCSs for helium using simple correlated wave functions and compared them with experiment. Calculations using the DWBA (Manson *et al.*, 1975; Manson, 1981) were made for 2-keV electron impact on helium. Bolorizadeh and Rudd (1986a) compared SDCSs for water vapor with calculations using the Mott equation, the Gryzinski equation, and the BEA. Oda (1973) gave a thorough review of both theoretical and experimental DDCSs available in 1973. In general, the theoretical treatments are more accurate for high incident energies than for low, for the intermediate range of angles (say, 30° to 110°) rather than the extreme forward or backward angles, and for simple atoms rather than for molecules or for atoms with inner shells. Most of the theoretical calculations fail at low incident energies.

Khare and collaborators (see, *e.g.*, Khare *et al.*, 1974; Khare and Meath, 1987; see also Section 3.3.2) have developed a semi-empirical model for the SDCSs. The model is based on a combination of the Born-Bethe and the Møller formulas and is obtained by multiplying each by an arbitrary factor and adding. The model has undergone several modifications; the one given in Khare and Meath (1987) may be written in different notation as

$$\sigma(\epsilon) = \frac{S}{NBt}\frac{t}{t+1}\left(1-\frac{w}{t-1)}\right)\frac{1}{w+1}\frac{df}{dw} \times \ln\left[1+c_i B(t-1)\right] + \frac{S}{Bt}\frac{t-1}{t(w^3-w_0^3)}\left(w-\frac{w^2}{t-w}+\frac{w^3}{(t-w)^2}\right), \quad (3.22)$$

where $w = \epsilon/B$, $t = T/B$, and $S = 4\pi a_0^2 N(R/B)^2$, $w_0 = W_0/B$ with N the number of electrons that participate in the collision, ϵ the secondary electron energy, T the primary electron energy, and B the ionization potential. W_0 is a mixing parameter which the authors suggest setting equal to 50 eV. The quantity $df/dw = B\ df/dQ$, where df/dQ is the differential oscillator strength for ionization. This quantity has been determined as a function of energy loss Q by photoionization measurements for many targets. An example of the results obtained with this equation is given for helium in Figure 3.33.

Rudd (1991) developed a semiempirical model yielding DDCSs, SDCSs, and TICSs for single-shell targets that satisfies all six of the consistency requirements described in Section 2.13. In this model, the angular distribution of electrons, both true secondary electrons from the target and scattered primaries, is represented by the sum of two Lorentzian peaks, the BE peak centered at an angle which depends on the

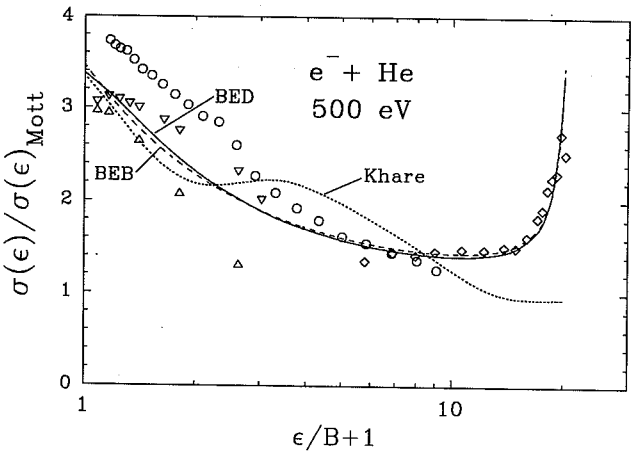

Fig. 3.33. SDCSs (divided by Mott cross sections to reduce the wide range of values) for 500 eV electrons on He. ○, Opal *et al.* (1971); ▽, Goruganthu and Bonham (1986); △, Müller-Fiedler *et al.* (1986); ◇, Oda (1975); full line, BED model; dashed line, BEB model; short dashed line, Khare and Meath (1987), Eq. 3.22.

primary and secondary electron energies, and a smaller backward peak centered at 180°. In this model, the DDCS, given in terms of the dimensionless variables $w = \epsilon/B$ and $t = T/B$, is

$$\sigma(w, \theta) = G_1 \left[\frac{1}{1 + \left(\frac{\cos\theta - G_2}{G_3} \right)^2} + \frac{G_4}{1 + \left(\frac{\cos\theta + 1}{G_5} \right)^2} \right] \tag{3.23}$$

The quantities G_1, G_2,. . . .,G_5 are adjustable parameters which are functions of w and t. The center of the binary peak, G_2, is found from momentum and energy considerations and is given by $G_2 = [(w + 1)/t]^{1/2}$. G_3 is the width of the binary peak which is approximated by $G_3 = 0.60[(1 - G_2^2)/w]^{1/2}$. The relative size of the backward peak is given by $G_4 = 10(1 - w/t)^3/[t(w + 1)]$. The value of G_5, the width of the backward peak, can be taken to be a constant equal to 0.33. G_1 is determined by equating the integral of the DDCS of Eq. 3.23 to the SDCS $\sigma(w)$. This yields

$$G_1 = \frac{\sigma(w)/2\pi}{G_3 \left[\tan^{-1}\left(\frac{1 - G_2}{G_3} \right) + \tan^{-1}\left(\frac{1 + G_2}{G_3} \right) \right] + G_4 G_5 \tan^{-1}\left(\frac{2}{G_5} \right)}. \tag{3.24}$$

An example of the application of Eqs. 3.23 and 3.24 is given in Figure 3.32.

The expressions for the SDCS and TICS given in the same paper may also be used, but require adjustable parameters which have only been determined for the two simple targets hydrogen and helium. However, the part of this model which yields SDCSs and TICSs has recently been superseded by a new model to be discussed next which provides reliable results for many targets at all energies without requiring adjustable fitting parameters.

3.6.2.1 Binary Encounter Dipole (BED) Model. A very promising development was reported by Kim and Rudd (1994) in constructing electron-impact SDCSs, $\sigma(\epsilon)$, and the resulting TICSs, σ_i. This method, known as the Binary Encounter Dipole (BED) model combines the dipole contribution with the BEA cross section. In the model, the ratios of the two contributions are chosen to make the asymptotic form of the TICS and the stopping cross section (the integral of the SDCS × energy transfer) consistent with the corresponding Bethe expressions. Using the quantities S, t, and w defined in the previous section and the reduced orbital kinetic energy $u = U/B$, where U is the orbital kinetic energy (see Section 2.5.1), the SDCS for a single shell is

$$\sigma(\epsilon) = \frac{S}{B} \left\{ F_1 \left[\frac{1}{w + 1} + \frac{1}{t - w} \right] + F_2 \left[\frac{1}{(w + 1)^2} + \frac{1}{(t - w)^2} \right] + \frac{F_3/N}{w + 1} \frac{df(w)}{dw} \right\}, \tag{3.25}$$

where

$$\begin{aligned} F_1 &= -F_2/(t + 1), \\ F_2 &= [2 - (N_i/N)]/(t + u + 1), \\ F_3 &= \ln t/(t + u + 1), \end{aligned} \tag{3.26}$$

with

$$N_i \equiv \int_0^\infty \frac{df(w)}{dw} dw. \tag{3.27}$$

To use this model, values of B, U, N, N_i and the continuum dipole oscillator strengths, $df(w)/dw$, are needed for each subshell of a target. The values of U for rare-gas atoms have been calculated from nonrelativistic Hartree-Fock wave functions. The expectation value U of the kinetic energy operator is a standard output in the Hartree-Fock wave function code published by Froese-Fischer (1991). The values of B, U and N for rare gas atoms and many common molecules are listed in Table 2.1. A more extensive table that covers additional molecules was given by Rudd *et al.* (1992).

Continuum dipole oscillator strengths from which N_i can be directly calculated are available from photoionization measurements. Compilations have been made, *e.g.*, by Berkowitz (1979) and by Gallagher *et al.* (1987; 1988). For convenience, continuum oscillator strengths of H, He, H_2 and Ne have been fitted to simple polynomials for use in generating SDCSs based on the BED model. The fitted coefficients are listed in Table 3.2 along with the values of N_i.

Available experimental data on SDCSs are not as reliable as those for TICSs. Nevertheless, the BED model reproduces all major features of the SDCSs for H, He, H_2, and Ne, which are mostly associated with the continuum dipole oscillator strengths of individual atoms and molecules. See, *e.g.*, the Platzman plot in Figure 3.34 for Ne.

The continuum dipole oscillator strengths of single-shell targets, H, He, and H_2, have an ϵ-dependence similar that of the BEAX equation (Eq. 2.12 of Section 2.5.2) which is the reason that BEAX cross sections seem to agree well with experiment for the single-shell targets. However, the BEA and BEAX formulas yield a less accurate ϵ-dependence of the SDCSs for multishell targets such as Ne and Ar.

3.6.2.2 Binary Encounter Bethe (BEB) Model. If the continuum dipole oscillator strengths for individual shells needed in the BED model are not available, one may use an approximation which eliminates the need for oscillator strength data and also

TABLE 3.2—*Coefficients for power series fit*[a] *to differential dipole oscillator strengths of H, He, H_2, and Ne*[b]

	H	He	H_2	Ne			
Coefficients	1s	1s	$1\varsigma_g$	2p, I[c]	2p, II[c]	2s	1s
a	0	0	0	4.8791	0	0	0
b	−0.022473	0	0	−2.8820	−5.8514	1.7769	0
c	1.1775	12.178	1.1262	−0.74711	329.30	2.8135	5.2475
d	−0.46264	−29.585	6.39820	0	−1678.8	−31.510	0
e	0.089064	31.251	−7.8055	0	3298.5	63.469	0
f	0	−12.175	2.1440	0	−2325.0	−52.528	0
g	0	0	0	0	0	15.982	0
B	13.6057	24.59	15.43	21.60	21.60	48.47	866.9
M_i^2	0.2834	0.489	0.680	1.552[d]	1.552[d]	0.04800	0.01642
N_i	0.4343	1.605	1.173	6.963[d]	6.963[d]	0.7056	1.686

[a] $df/d(Q/B) = ay + by^2 + cy^3 + dy^4 + ey^5 + fy^6 + gy^7$, where $y = B/Q$ with B the binding energy and Q the photon energy, or the energy transfer.

[b] Data on H_2 and Ne from Berkowitz (1979), and for He from Marr and West (1976).

[c] Ne(2p, I) covers photon energies from the 2p ionization threshold (21.60 eV) to the 2s ionization threshold (48.47 eV), and Ne(2p, II) covers photon energies above 48.47 eV.

[d] Values for 2p(I + II).

simplifies the model. The simplified version, known as the Binary Encounter Bethe (BEB) model, results from approximating the series expansion of the differential oscillator strength df/dQ with the first term. The result given by Kim and Rudd (1994) is

$$\sigma(w) = S \sum_{n=1}^{3} F_n(t)[f_n(w+1) + f_n(t-w)], \quad (3.28)$$

where

$$f_n(w+1) = (w+1)^{-n}, \quad f_n(t-w) = (t-w)^{-n} \quad (3.29)$$

and

$$\begin{aligned} F_1 &= -F_2/(t+1), \\ F_2 &= 2(1-\Gamma)/(t+u+1), \\ F_3 &= \Gamma \ln t/(t+u+1). \end{aligned} \quad (3.30)$$

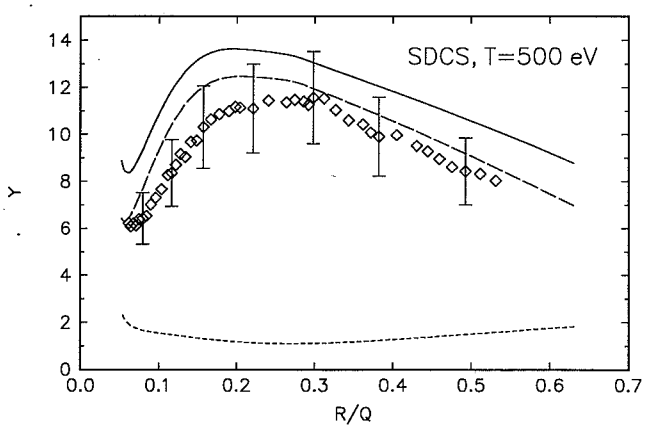

Fig. 3.34. Platzman plot (see Section 2.9) of ionization of Ne by 500-eV incident electrons. Full curve, total BED model result; long dashed and short dashed lines, 2p and 2s subshell contributions calculated by the BED model; ◇, experimental data of Opal *et al.* (1972). The BED model leads to a total ionization cross section which is 3% higher than the experimental value by Rapp and Englander-Golden (1965).

The quantity Γ is given by

$$\Gamma = 2BM_i^2/NR, \quad (3.31)$$

where M_i^2, the square of the dipole matrix element for ionization, is defined as

$$M_i^2 = \frac{R}{B_1}\int_0^\infty \frac{1}{w+1}\frac{df(w)}{dw}\,dw. \quad (3.32)$$

M_i^2 values are often available even when differential oscillator strength information is not. But when even those quantities are unavailable, one can make the further approximation of setting $\Gamma = 1$ for each subshell. Note that Eq. 3.28 must also be summed over subshells.

3.6.2.3 Integration of the BED and BEB Equations. The SDCS BED model just described may be integrated to provide a compact, analytic equation for the TICS. Integrating Eq. 3.25 over w, actually from $w = 0$ to $w(\max) = (t-1)/2$, we get a simple expression for $\sigma_i(t)$ for all t

$$\sigma_i(t) = \frac{S}{t+u+1} \times \left[D(t)\ln t + \left(2 - \frac{N_i}{N}\right)\left(\frac{t-1}{t} - \frac{\ln t}{t+1}\right)\right], \quad (3.33)$$

where the function $D(t)$ is defined by

$$D(t) \equiv \frac{1}{N}\int_0^{(t-1)/2} \frac{1}{w+1}\frac{df(w)}{dw}\,dw. \quad (3.34)$$

The cross section must be summed over the subshells that contribute to ionization. Note that Eq. 3.33 has the same asymptotic form as the Bethe theory since by definition (Eq. 3.32) $M_i^2 \propto D(t)$ in the limit $t \to \infty$. The advantages of the BED formula for σ_i over the Bethe theory—or variations of the Bethe theory—are that the BED formula (a) approaches the low incident

energy region with an appropriate threshold behavior; (b) includes the interference term between the direct and exchange interactions, which introduces the $\ln t/(t+1)$ term; and (c) includes the dipole contribution $D(t)$ which decreases as t decreases. In Figure 3.35, we compare the experimental $\sigma_i(T)$ for atomic hydrogen (Shah *et al.*, 1987) with that derived from the BED model. Note that the BED model does not contain any empirical or adjustable parameters. The polynomial fit to $df(w)/dw$ used in the BED model is merely to simplify, for convenience, a more complicated but exact theoretical expression. The TICSs based on the BED model for some simple atoms also agree well (±10% in most cases) with accurate measurements.

Similarly, the BEB model, Eq. 3.28, leads to the TICS equation:

$$\sigma(T) = \frac{S}{t+u+1}\left\{\frac{\Gamma}{2}(1-1/t^2)\ln t + (2-\Gamma) \times \left[(1-1/t) - \frac{\ln t}{t+1}\right]\right\}. \quad (3.35)$$

For applications in which only TICSs are needed, or to renormalize a SDCS constructed from a theoretical model for better accuracy, σ_i can be fitted to even simpler functions of t than those used in Eq. 3.33 or 3.35 by omitting the summation over subshells and using a single $t \equiv t_1 = T/B_1$, where the subscript 1 indicates the outermost or least tightly bound subshell. When reliable values of σ_i are known—usually through very accurate measurements—then a simple form to fit σ_i for electron-impact ionization is

$$\sigma_i(t) = \frac{4\pi a_0^2 Z_1^2}{t}\left[a\ln t + b\left(1-\frac{1}{t}\right) + c\frac{\ln t}{t+1}\right], \quad (3.36)$$

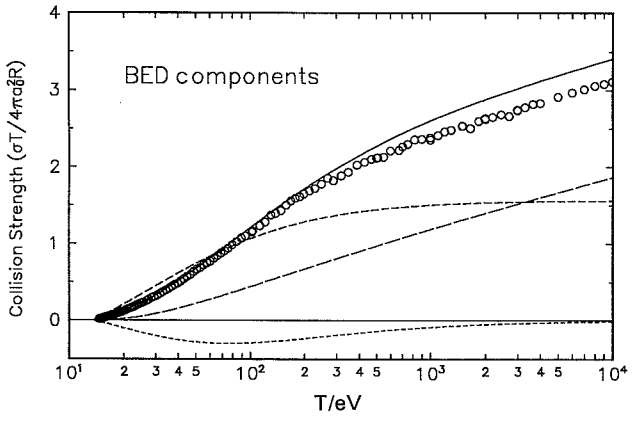

Fig. 3.35. Fano plot (see Sec. 2.13) for the electron-impact ionization of H. ○, experimental data by Shah *et al.* (1987); full curve, BED model. Various components that contribute to the BED cross section are also shown: long dashed line, dipole contribution (last term in Eq. 3.25); medium dashed line, hard collision contribution (second term); short dashed line, interference term (first term).

where a, b, and c are fitting coefficients. We have eliminated any reference to the reduced kinetic energy u to make the fitting formula simple. Also, theoretical cross sections are often presented in terms of the collision strength, which is customarily defined as $\sigma_i E/\pi a_0^2 R$, and the elimination of u in Eqs. 3.36 and 3.37 below makes comparisons with other theoretical results simpler. Note that the first ln t in Eq. 3.36 arises from the dipole interaction (which dominates in a distant collision), while the second ln t results from integrating the interference term in the Mott formula (which describes a close collision). If this three-term fit is insufficient, then we can add more terms with additional fitting coefficients, d, e, and so on:

$$\sigma_i(t) = \frac{4\pi a_0^2 Z_1^2}{t}\left[a\ln t + b\left(1-\frac{1}{t}\right) + c\frac{\ln t}{t+1} + d\frac{\ln t}{(t+1)^2} + e\frac{\ln t}{(t+1)^3} + \cdots\right]. \quad (3.37)$$

As expected, σ_i for multishell targets requires more fitting parameters than targets with simple structures. Parameters for fitting Eq. 3.37 for a few examples are listed in Table 3.3. Note that Eq. 3.37 can also be adapted to ionizations that take place without appreciable dipole interaction—*e.g.*, double ionization of He—by dropping the first term.

3.6.3 Recommended Differential Cross Sections

Table 3.4 lists the experiments which measured differential ionization cross sections for various target gases. There have been very few compilations or critical reviews of such data. McDaniel *et al.* (1977-79) have compiled SDCSs for various targets of interest to high energy laser work. Kim (1983b) made a study of existing experimental data on helium, judging them on the basis of the consistency criteria described in Sections 2.13 and 3.3.3. He fitted a Legendre polynomial series to the angular distributions at selected secondary energies, thus providing recommended values of the DDCSs for helium.

The consistency requirements can be applied to judge the accuracy of data or of cross sections calculated by theoretical methods or by analytical models. Platzman plots, discussed in Section 2.9, and Fano

TABLE 3.3—*Parameters for fitting Eq. 3.37 to total ionization cross sections of H, He, H_2 and Ne*

	H	He	H_2	Ne
a	0.233	0.668	0.541	2.36
b	1.58	3.15	4.14	6.25
c	−2.69	−7.03	−10.8	−30.6
d	−0.850		14.3	50.2
e			−20.2	−45.9

TABLE 3.4—*Experimental electron-impact singly and doubly differential cross sections*

Investigators	Incident energy eV	Ejected electron Energy eV	Ejected electron Angle degrees
Hydrogen (H)			
Shyn (1992)	25–250	1-(T-B)/2	12–156
Helium (He)			
Mohr and Nicoll (1934)	20–100	0-(T-B)	20–155
Goodrich (1937)	100	1-(T-B)	2.5–164
Ehrhardt *et al.* (1971)	25–260	1.5-(T-B)	3–125
Opal *et al.* (1971, 1972)	50–2000	4-(T-B)/2	30–150
Oda and Nishimura (1971, 1977) and Oda (1973)	500, 1000	4-(T-B)	15–148
Oda *et al.* (1972)	500	4-(T-B)	15–148
Grissom *et al.* (1972)	150	0–1	all
Sethuraman *et al.* (1972)	50–500	4-(T-B)	10–150
Rudd and DuBois (1977)	100, 200	3-(T-B)	10–150
Shyn and Sharp (1979a)	50–300	1-(T-B)/2	6–156
Goruganthu and Bonham (1986)	200–2000	2–50	30–150
Müller-Fiedler *et al.* (1986)	100–600	2-(T-B)	3–150
Nasir *et al.* (1989)	100	40	40–110
Neon (Ne)			
Mohr and Nicoll (1934)	20–100	0-(T-B)	20–155
Opal *et al.* (1971, 1972)	500	4–200	30–150
Grissom *et al.* (1972)	150	0–1	all
DuBois and Rudd (1978)	100–500	4-(T-B)	10–150
Argon (Ar)			
Mohr and Nicoll (1934)	20–100	0-(T-B)	20–155
Vroom and Comeaux (1971)	1000–10,000	0–600	7.5–172.5
Ehrhardt *et al.* (1971)	25–260	1.5-(T-B)	3–125
Opal *et al.* (1971, 1972)	500	4–200	30–150
Grissom *et al.* (1972)	150	0–1	all
Mathis and Vroom (1976)	1000	4–500	90
DuBois and Rudd (1978)	100–500	4-(T-B)	10–150
Nasir *et al.* (1989)	100	40	40–110
Krypton (Kr)			
Opal *et al.* (1971, 1972)	500	4–200	30–150
Oda *et al.* (1972)	1000	21–52	10–130
Xenon (Xe)			
Opal *et al.* (1971, 1972)	500	4–200	30–150
Mercury (Hg)			
Mohr and Nicoll (1934)	20–100	0-(T-B)	20–155
Hydrogen (H_2)			
Mohr and Nicoll (1934)	20–100	0-(T-B)	20–155
Opal *et al.* (1971, 1972)	500	4–200	30–150
DuBois and Rudd (1978)	100	4-(T-B)	10–150
Shyn *et al.* (1981)	25–250	1-(T-B)/2	12–156
Rudd *et al.* (1993)	200–1500	5-(T-B)	15–150
Nitrogen (N_2)			
Mohr and Nicoll (1934)	20–100	0-(T-B)	20–155
Vroom and Comeaux (1971)	1000–10,000	0–600	7.5–172.5
Opal *et al.* (1971, 1972)	50–2000	4–200	30–150
Tisone (1972a)	500–1000	5–500	40–115
Mathis and Vroom (1976)	1000	4–500	90
DuBois and Rudd (1978)	100–500	4-(T-B)	10–150
Shyn (1983)	50–400	1-(T-B)/2	12–156
Goruganthu *et al.* (1987)	200–2000	2–50	30–150
Nasir *et al.* (1989)	100	40	40–110
Oxygen (O_2)			
Opal *et al.* (1971, 1972)	50–2000	4–200	30–150
Tisone (1972b)	500	30–110	6–30
Shyn and Sharp (1991)	25–250	1-(T-B)/2	12–156
Methane (CH_4)			
Mohr and Nicoll (1934)	20–100	0-(T-B)	20–155
Opal *et al.* (1971, 1972)	500	4–200	30–150
Oda and Nishimura (1975)	500, 1000	4-(T-B)	15–148
Oda (1975)	500	4-(T-B)	15–148
Ammonia (NH_3)			
Opal *et al.* (1971, 1972)	500	4–200	30–150
Water vapor (H_2O)			
Opal *et al.* (1971, 1972)	500	4–200	30–150
Oda (1975)	500, 1000	4-(T-B)	15–148
Oda and Nishimura (1975)	500, 1000	4-(T-B)	15–148
Mathis and Vroom (1976)	1000	4–500	90
Vroom and Palmer (1977)	1000–10000	0.5–200	30–150
Bolorizadeh and Rudd (1986)	50–2000	2-(T-B)	15–150
Hollman *et al.* (1988)	1500	2-(T-B)	15–150
Water clusters ($(H_2O)_n$)			
Mathis and Vroom (1976)	1000	4–500	90
Acetylene (C_2H_2)			
Opal *et al.* (1971, 1972)	500	4–200	30–150
Carbon Monoxide (CO)			
Opal *et al.* (1971, 1972)	500	4–200	30–150

TABLE 3.4—*Continued*

Investigators	Incident energy eV	Ejected electron Energy eV	Ejected electron Angle degrees
Tisone (1972b)	500	30–110	6–30
Oda and Nishimura (1975)	500, 1000	4-(T-B)	15–148
Oda (1975)	500	4-(T-B)	15–148
Ma and Bonham (1988)	800	9–393	30–150
Nasir *et al.* (1989)	100	40	40–110
Nitrous Oxide (NO)			
Opal *et al.* (1971, 1972)	500	4–200	30–150
Carbon Dioxide (CO_2)			
Opal *et al.* (1971, 1972)	500	4–200	30–150
Shyn and Sharp (1979b)	50–400	1-(T-B)/2	12–156
Nasir *et al.* (1989)	100	40	40–110

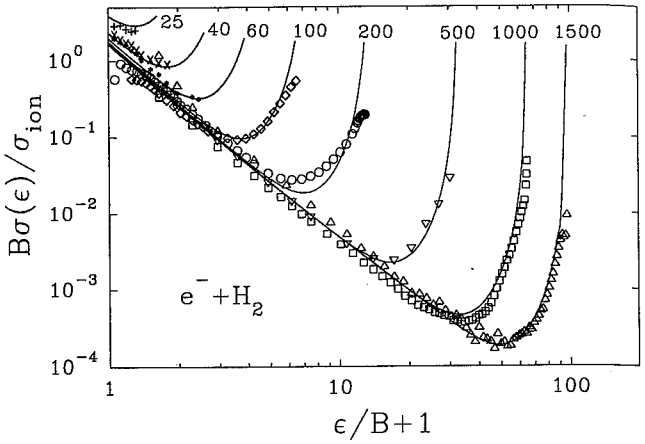

Fig. 3.36. Plots of SDCSs from electron impact on molecular hydrogen at energies from 25 to 1500 eV. Data at 25, 40, and 60 eV, Shyn *et al.* (1981); data at 100 eV, DuBois and Rudd (1978); data at 200, 500, 1000, and 1500 eV, Rudd *et al.* (1993); full lines, BEB model, Eqs. 3.28-3.32. Data above 100 eV incident energy approaches a universal curve for $\epsilon < (T - B)/2$.

plots, described in Section 2.13 are helpful in assessing data and have been used, *e.g.*, by Paretzke (1987) to analyze SDCS data on water vapor.

Another type of graph which is useful in comparing SDCS data for simple targets at various energies was introduced by Rudd *et al.* (1993). Define the dimensionless quantity

$$X(w) = \frac{B\sigma(w)}{\sigma_i} . \qquad (3.38)$$

Then from Eqs. 3.28 and 3.35 for $t \gg 1$ and $w < t/2$,

$$X(w) \simeq \frac{J_2(t)}{(w+1)^2} + \frac{J_3(t)}{(w+1)^3} , \qquad (3.39)$$

where $J_2(t)$ and $J_3(t)$ are slowly varying functions of t which asymptotically approach constants for large t. If we plot $X(w)$ versus $w + 1$ on a log-log scale, we get the sum of two straight lines with slopes of -2 and -3. The combination, in fact, is not far from a straight line (for small w) and, since J_2 and J_3 are both nearly constant, the plot should be a universal curve for all (sufficiently high) primary energies. Furthermore, for the targets for which the BEB approximation is valid the graphs will be the same for different targets as well. If accurate values of σ_i are available, such graphs also provide a good check on the normalization of the experimental SDCS data. Examples are given in Figure 3.36.

Since the BED and BEB models do not require as input any cross section data and have no fitting parameters, they may be used to predict SDCSs and TICSs for any target for which binding energies, orbital kinetic energies, and dipole oscillator strengths are known at least for the outer subshells. The DDCS model described by Eqs. 3.23 and 3.24 may be useful in describing the angular distributions of electrons, but so far it has only been tested for hydrogen and helium.

4. Ion Interactions

4.1 Introduction

Electron production in ion-atom collisions has received a great deal of attention because of its importance in basic as well as applied research. The Rutherford formula (Eq. 2.3) is of fundamental importance for the binary collision mechanism in which the only interaction considered is the one between the target electron and the incident projectile. This two-body process is treated in the classical BEA (*e.g.*, Gryzinski, 1959; 1965; Vriens, 1967), which has found wide application in the field of ion-induced electron production. Bethe (1930) used the Born approximation to describe electron emission by charged particles (see Section 2.8). For the hydrogen target, he derived a closed form expression for the differential ionization cross section as a function of the momentum transfer and the energy and angle of the ejected electron (Landau and Lifschitz, 1958).

Only a few measurements of the spectra of ion-ejected electrons were made before 1960. Blauth (1957) and Moe and Petsch (1958) were the first to measure energy distributions of electrons produced in ion-atom collisions but only for a limited number of observation angles. In the 1960s, Kuyatt and Jorgensen (1963), Rudd and Jorgensen (1963) and Rudd *et al.* (1966b) started a series of measurements of absolute differential cross sections in which nearly complete energy and angular distributions were measured for the first time. Experiments were also performed using heavy-ion impact at relatively low impact energies by Cacak and Jorgensen (1970). After 1970, extensive studies were made at several other laboratories, e.g., Toburen (1971; 1974), Toburen and Wilson (1972), and Stolterfoht (1971a; 1971b).

In this section, we first discuss the major mechanisms that contribute to secondary electron emission in ion-atom collisions. Then, the experimental techniques for measuring differential cross sections are described, followed by theoretical and semi-empirical methods for their calculation. Recommended methods for obtaining values of total and differential ionization cross sections are then given for proton impact. Some of the effects characteristic of heavy-ion impact are next described. Although helium ions are included, emphasis is given to projectile ions with higher nuclear charges. Since heavy incident ions are generally "dressed" (*i.e.*, carrying electrons), ionization of the projectile will also be discussed. Because of the many possible combinations of targets and the types, charge states, and energies of the projectiles, the situation for ion impact is very complicated and the subject is far from completely explored. As a result, except for proton impact, not enough data on ion impact has accumulated yet to allow us to recommend values of cross sections in a systematic way.

4.2 Mechanisms of Ionization by Ion Impact

4.2.1 Zero-, One-, and Two-Center Electron Emission

In discussing the emission of electrons in heavy ion-atom collisions, we will adopt an intuitive picture in which we view the process in terms of *collision centers* which are formed by strongly interacting heavy particles. Formally, a center is associated with an ion core whose interaction with an electron requires a description beyond first-order perturbation theory. The principles of the center picture are schematically displayed in Figure 4.1 which shows the removal of a target electron by means of a small perturbation originating from an incident ion.

In the *zero-center* case the trajectory of the electron is not significantly affected by either the target or the projectile and thus follows a straight-line trajectory. This is referred to as binary-encounter (BE) electron emission and can be described by a classical binary-encounter theory (Thomas, 1927; Gryzinski, 1959; 1965; Bonsen and Vriens, 1970) or by the Born approximation using a plane wave for the final continuum electron.

If the interaction of the electron with only one of the collision partners can be neglected, the ionization process is referred to as *single-center electron emission* (SCEE). In this case, either the projectile or the target can form a center. In the example in Figure 4.1, the SCEE process first involves a BE event, followed by a scattering of the outgoing electron in the Coulomb field of the target nucleus. Soft collisions (those involving a small momentum transfer) at high energies are described by the first Born approximation with initial and final states centered at the target

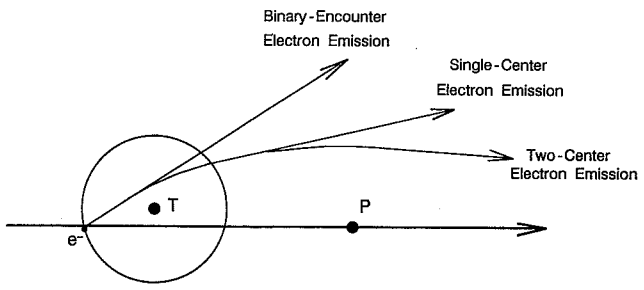

Fig. 4.1. Mechanisms for electron emission associated with different trajectories. *Binary encounter* refers to a two-body interaction between the projectile and the target electron. In single-center electron emission the electron is affected by the nuclear field of the target. In two-center electron emission the electron is affected by the fields of both the target and the projectile nuclei.

nucleus (see Bates and Griffing, 1953 and Sections 2.6 and 2.7).

If both collision partners play a significant role in the collision (Stolterfoht *et al.*, 1987), the ionization process is *two-center electron emission* (TCEE). This is a three-body problem for which methods employing approximations are required. Figure 4.2 provides evidence for some of the characteristic electron production mechanisms. Two-center effects are visible in the spectrum between the soft collision peak and the BE maximum. TCEE is most evident with high-energy projectiles where there is a large separation between the soft and BE peaks. However, as the incident energy is decreased, the BE peak becomes less prominent and the two overlap more and more, finally merging as shown in Figure 4.3. TCEE effects are most easily seen in the DDCSs. Since the SDCSs are governed by BE and soft collisions which are one-center phenomena, they are less affected by TCEE. The BE peak does not show up in the SDCS spectrum because, as shown in Figure 4.4, it is the sum of overlapping BE maxima the energies of which vary continuously with emission angle.

The interaction of the outgoing electron with the projectile results in an enhancement of the electron emission at forward angles. This two-center effect is evident when experimental ionization cross sections are compared with the results of the Born approximation which is based on the single-center picture. Enhanced electron emission was observed at 10° by Rudd and Jorgensen (1963) and at 0° by Harrison and Lucas (1970) and Crooks and Rudd (1970). The effect was described theoretically by Salin (1969, 1972) and was interpreted by Macek (1970) as an electron capture to a continuum state of the projectile (ECC). Classically, one may think of it as a Coulomb focusing

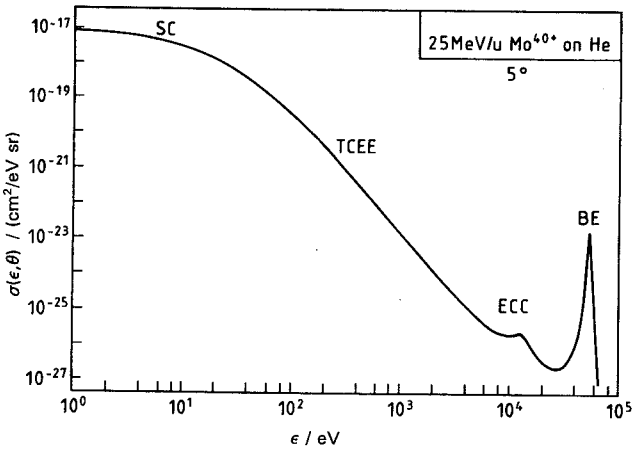

Fig. 4.2. Typical electron spectrum demonstrating the different mechanisms for electron production. SC, soft collision; TCEE, two-center electron emission; ECC, electron capture to the continuum; BE, binary encounter. The data, referring to electron emission at 5° in collisions of 25-MeV/u Mo^{40+} on He, were calculated by means of the CDW-EIS approximation (from Stolterfoht *et al.*, 1987).

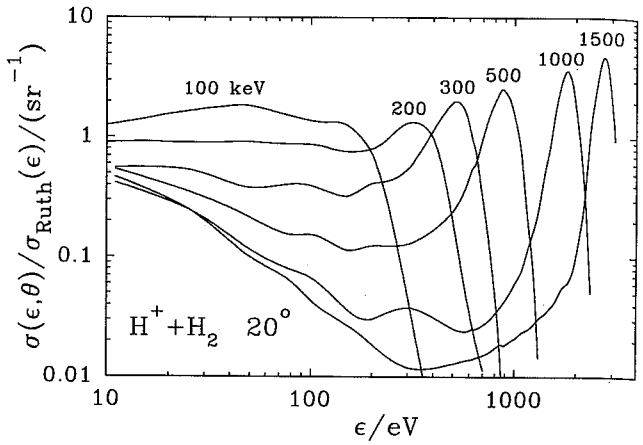

Fig. 4.3. Energy distribution of secondary electrons ejected at 20° from $H^+ + H_2$ collisions at various incident energies. Note the increasing prominence of the binary peak at the higher energies.

of outgoing electrons. The forward peak is cusp-shaped and appears in the spectrum where the secondary electron has the same velocity as the projectile ion. Reviews of ECC include those by Rudd and Macek (1972), Sellin (1982), Lucas, *et al.* (1984), and Briggs (1989).

Recently, studies have been made of the so-called "saddle-point electrons" stranded in the potential minimum along the axis between the target and projectile (Meckbach *et al.*, 1986; Olson, 1986; Olson *et al.*, 1987; Gay *et al.*, 1990; DuBois, 1993). This

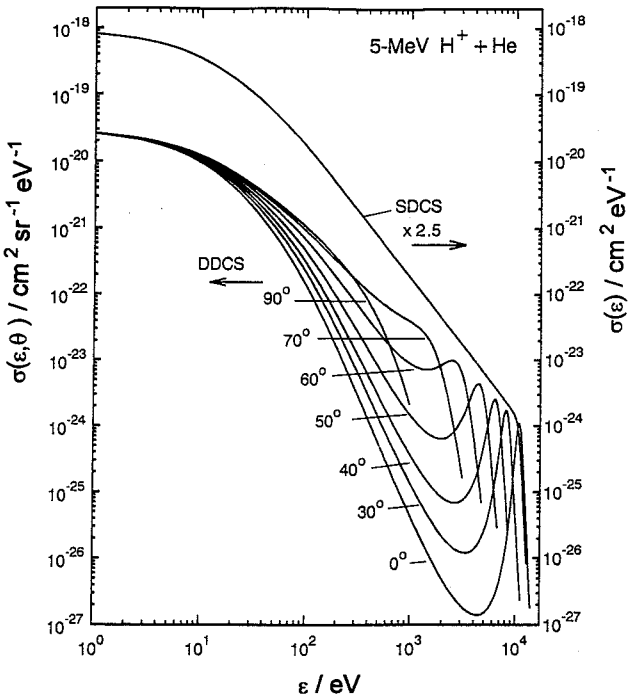

Fig. 4.4. SDCSs and DDCSs for electron emission at different angles in 5-MeV $H^+ + He$ collisions. The data are calculated using the HKS-model. The binary encounter maxima in the DDCSs combine to make a smooth SDCS curve.